TOPICAL REPORT
Project No.: 9-61-5329

ORNL/Sub/89-SA187/01

TITLE: LITERATURE SEARCH UPDATE FIRESIDE CORROSION TESTING OF CANDIDATE SUPERHEATER TUBE ALLOYS, COATINGS, AND CLADDINGS

Authors: S. Van Weele and J. L. Blough

September 1990

Report Prepared by:

FOSTER WHEELER DEVELOPMENT CORPORATION
12 Peach Tree Hill Road
Livingston, New Jersey 07039

Prepared for:

OAK RIDGE NATIONAL LABORATORY
Oak Ridge, Tennessee 37831

Operated by:

MARTIN MARIETTA ENERGY SYSTEMS, INC.
for the
U. S. DEPARTMENT OF ENERGY

Under Contract No.:

DE-AC05-84OR21400

FOSTER WHEELER DEVELOPMENT CORPORATION
Livingston, New Jersey 07039

ORNL/Sub/89-SA187/01

LITERATURE SEARCH UPDATE FIRESIDE CORROSION TESTING OF CANDIDATE SUPERHEATER TUBE ALLOYS, COATINGS, AND CLADDINGS

Authors:

S. Van Weele
J. L. Blough

September 1990

Research sponsored by the U.S. Department of Energy,
Fossil Energy
Advanced Research and Technology Development Materials Program

Report Prepared by
FOSTER WHEELER DEVELOPMENT CORPORATION
12 Peach Tree Hill Road
Livingston, New Jersey 07039

under
ORNL/Sub/89-SA187/01

for

OAK RIDGE NATIONAL LABORATORY
Oak Ridge, Tennessee 37831
operated by
MARTIN MARIETTA ENERGY SYSTEMS, INC.
for the
U. S. DEPARTMENT OF ENERGY
under Contract No. DE-AC05-840R21400

Tables

Number		Page
1	Relationship of Corrosion Rates to Chlorine Content	2
2	Alloys Currently Being Tested in Corrosion Probes in Utility Boilers	4
3	Preliminary Data From Destructive Examinations of Corrosion Probes After 4000 Hours	5
4	Commercial Steels and Alloys Studied During EPRI's Fireside Corrosion Project	13
5	Coatings Studied During EPRI's Fireside Corrosion Project	14
6	Average Corrosion Losses After 48-Hour Exposure	16
7	Performance of Coatings After Repeated Cycles	16
8	Ash Composition and Corrosion Losses During Testing at 1292°F	18
9	Results of Coal Ash Corrosion Test on Cr-Ni-Fe Ternary Alloys	19
10	Weight Loss Data for Tests at 1292°F (700°C) for 100 Hours	20
11	Chemical Composition of Alloy for Corrosion Tests	21
12	Chemical Composition of Tube Alloys	24
13	Chemical Composition of Cladding Alloys	25
14	Chemical Composition of Welding Alloys	25

Figures

Number		Page
1	Corrosion From Alkali-Sulfur Compounds	1
2	Composition Drawing of Ternary System Na_2SO_4-K_2SO_4-$Fe_3(SO_4)_3$	6
3	Normalized Weight Gain Curves for Oxidation of Steels in Molten Sulfate Corrected for Volatilization of Alkali Sulfates	7
4	Phase Stability Diagram of Fe-O-S at 1292°F (700°C)--Point A Corresponds to the Equilibrium Gas Composition	9
5	Reaction of Nickel with Na_2SO_4 Layer (2.5 mg/cm^2) With 1 atm O_2 + 4% SO_2 at 1220 to 1652°F	10
6	Reaction of Nickel With 1 atm O_2 + 4% SO_2 at 1220 to 1652°F	10
7	Results of Fireside Corrosion of Commercial Alloys	15
8	Results of Fireside Corrosion of Commercial Stainless Steel	15
9	Alloy Modification of Type 347 for Fireside Corrosion Test Cycles	15
10	Effect of MoO_3 Addition to Ash B on Corrosion Loss of 347H at 700°C for 25 Hours in 0.25%SO_2 Flue Gas	17
11	Corrosion Loss - Time Curves for 17-14 CuMo and 347H at 700°C in Ash B as a Function of SO_2 Content of Flue Gas	17
12	Effect of Chromium on Synthetic Coal-Ash Corrosion Loss of Ni-Cr-Fe Alloys at 1292°F (700°C) for 100 Hours	19
13	Effect of Iron on Synthetic Coal-Ash Corrosion Loss of 34 or 40 Cr-Ni-Fe Alloys at 1292°F (700°C) for 100 Hours	19
14	Synthetic Coal-Ash Corrosion of Alloy CR35A and Commercial Alloys	20
15	Corrosion rate in Coal Ash Corrosion Test for Various Alloys	21
16	Corrosion Rate in Coal Ash Corrosion Tests for Various Cladding Alloys an Nickel Based Alloys	21
17	Weight Loss Per Unit Area vs. Temperature (A213 T-22)	23
18	Weight Loss Per Unit Area vs. Temperature (HT-91)	23

Figures

Number		Page
19	Effect of Temperature on the Corrosion Rate of Ni-30Cr, Coated With 2.5 mg/cm^2 of Na_2SO_4, in O_2-1% (SO_2 + SO_3)	23
20	Effect of Temperature on the Corrosion Rate of Co-30Cr, Coated With 2.5 mg/cm^2 of Na_2SO_4, in O_2-0.15% (SO_2 + SO_3)	24
21	Average Weight Loss/Test Temperature Curves (Type 1)	26
22	Average Weight Loss/Test Temperature Curves (Type 2)	26
23	Average Weight Loss/Test Temperature Curves (Type 3)	26
24	Average Weight Loss/Test Temperature Curves (Type 4)	27
25	Average Weight Loss/Test Temperature Curves (Type 5)	27
26	Effect of Alkali Sulfate Content on Corrosion Loss in 0.25 vol% SO_2 and 4 vol% O_2 Gas at 1202°F (650°C) for Type 347H, 17-14 CuMo, Type 310SS, and Alloy 800H	28
27	Effects of SO_2 Content on Corrosion Loss in 5 wt% Alkali Sulfates Ash at 1202°F (650°C) for Type 347H, Type 310SS, 17-14 CuMo, and Alloy 800H	28
28	Relationship Between Chromium Content of Alloys and Relative Corrosion Loss in 4 vol% O_2 at 1292°F	30
29	Isocorrosion Diagram of 17-14 CuMo at 1112°F	31

Section 1

INTRODUCTION

Attack of fireside surfaces by ash deposits has been a concern of boiler manufacturers and operators for many years. Widespread coal-ash corrosion problems in superheater and reheater tubes in large central-station boilers began after the introduction of higher steam temperatures in the 1940s. From the 1950s to the present, boiler manufacturers and operators have reduced corrosion rates to an acceptable level by keeping steam temperatures below 1050°F (565°C) or by burning coal blends with low sulfur and alkali contents [1].*

In recent years concern for increased thermal efficiency in power generation has brought renewed interest in raising steam temperatures to the ultra-supercritical regime. New supercritical boiler designs could push steam temperatures as high as 1200°F (650°C) [2]. Low-sulfur low-alkali coals have become scarcer and more expensive; the ability to burn poor-quality coal would lower fuel costs and stretch energy supplies. Many stations will be forced by economic necessity to burn a variety of coals.

This report† updates and supplements the literature reviews "Corrosion Problems in Coal Fired Boiler Superheater and Reheater Tubes" [3] and "Fireside Corrosion of Superheater Alloys for Advanced Cycle Steam Plants" [4]. It also summarizes the progress made during the decade since Rehn's original literature review (1979-1989) toward understanding the mechanisms of coal-ash corrosion and the advances made in combatting this corrosion problem. The corrosion of concern in this report is coal-ash attack of superheater and reheater tubes caused by alkali-iron trisulfates in the temperature range between 1100 and 1400°F (593 and 760°C) [3]. This type of attack is distinct from both the lower-temperature pyrosulfate-induced corrosion and high-temperature [≥1500°F (815°C)] gaseous attack, as shown in Figure 1 [5]. High-temperature attack in gas turbines, corrosion problems in oil-fired boilers, and corrosion in coal-conversion systems are not included.

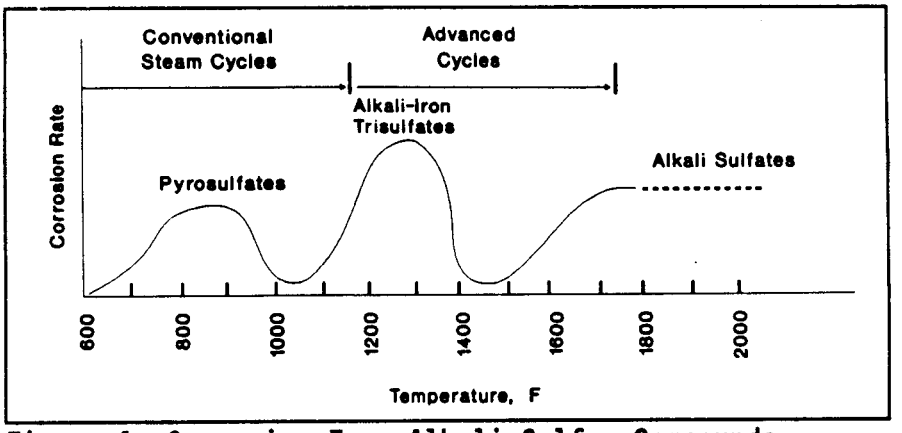

Figure 1 Corrosion From Alkali-Sulfur Compounds

*References are listed in Section 6.

†Research sponsored by the U.S. Department of Energy, Fossil Energy AR&TD Materials Program, DOE FEAA1510100, Work Breakdown Structure Element FW-2.

Section 2

PLANT EXPERIENCE/IN-SITU TEST PROBE

Corrosion of pulverized-coal-fired boilers in the United Kingdom has been reviewed by Meadowcroft [6] and by Flatley and Morris [7]. The coals have high chloride and moderate sulfur contents; fireside metal temperatures range up to 1220°F (660°C). Final superheater and reheater tubes are manufactured from austenitic stainless steels, commonly Types 304, 316, 321, and 347, and Esshete 1250. No significant differences in corrosion rates have been found between these steels when the station burns low-alkali-containing coals. In stations burning high-alkali-containing coals, coextruded tubes of either Type 310/Esshete 1250 or IN 671/Incoloy 800 have been found to have corrosion rates one-third and one-tenth of Type 316 respectively.

Latham, Flatley, and Morris surveyed the corrosion resistance of superheater materials using both air-cooled probes and tubes placed in situ into superheater pendants [8]. Fireside metal temperatures ranged between 1112 and 1292°F (600 and 700°C), with flue gas temperatures between 1652 and 2192°F (900 and 1200°C). Corrosion rates of steels in superheaters burning coals with varying chlorine contents are listed in Table 1. Both probe trials and in-situ trials ranked the alloys in the same order for corrosion resistance. Alloys showed a decreasing corrosion rates in this order:

IN671 < Type 310 < Type 347 < Type 316 < Esshete 1250

Table 1 Relationship of Corrosion Rates to Chlorine Content

Description	Hours in Service (x 1000)	Corrosion Rate mils/yr	Corrosion Rate nm/h
0.15% Chlorine Coal:			
Type 347	29.0	15	50
Type 310/Esshete 1250	29.0	1.7	6
0.30% Chlorine Coal:			
Type 316		29	100
Type 310/Esshete 1250	29.0	16	55
0.45% Chlorine Coal:			
Esshete 1250	6.0	58	200
Type 316	15.4	46	160
Type 347	15.4	58	200
Type 310/Esshete 1250	18.0	17	60
Inconel 671/Incoloy 800	34.0	negligible	

The chloride content of the coal influenced the aggressiveness of the attack. Coal containing 0.15 percent chlorine produced a 1.7-mils/yr (6-nm/h) corrosion rate on IN671, while 0.30 percent and 0.45 percent chlorine coals produced a 17 mils/yr (60 nm/h) corrosion rate on the same alloy. Chlorine has been implicated as a factor in scale cracking and is known to promote the release of alkalies.

Balting, et al., reviewed the performance of IN671/IN800 coextruded tubes [9]. After 1 year of service, these tubes suffered 1 mil/yr (3.4 nm/h) corrosion loss. Surrounding tubes constructed of a 12%Cr-1%Mo-0.3%V steel corroded at 30 mils/yr (102 nm/h).

Meadowcroft mentions in his review of coal-fired boiler practice in the United Kingdom that 50%Cr-50%Ni/IN800 composite tubes suffered negligible corrosion rates in superheaters [10]. These tubes were produced using powder metallurgy. In a related article, Chandler and Quigley state that plasma-sprayed 50%Cr-50%Ni has been undergoing tests in boilers and shows no corrosion losses or spalling [11]. An FeCrAl alloy, also tested as a plasma spray coating, showed little corrosion.

Additives to the coal feed to reduce corrosion and sulfur-trioxide levels in coal-fired boilers have met with limited success. Locklin, et al., reviewed additive trials by utilities [12]. Magnesia was added to coal at up to 1200 ppm. With the additive, SO_3 levels were reduced and convective surfaces seemed cleaner. However, the cost and handling of additives have prohibited their use by utilities.

Chromized 17-14 CuMo tubing and Type 310 clad 17-14 CuMo tubing were investigated by DeLong, et al., as an alternative for bare 17-14 CuMo tubing in the superheater section of Eddystone Unit 1 [13]. Stress levels in the superheater and restrictions on the tubewall thickness mandated the use of 17-14 CuMo tubing or an alloy with the same strength. The wastage rates of bare 17-14 CuMo as a result of coal-ash corrosion were unacceptably high. To mitigate the corrosion wastage rate while retaining the desirable properties of 17-14 CuMo, a clad layer of Type 310 stainless steel and a chromized layer were selected. Sections of the coated tubes were mounted in the superheater beside tubes of bare 17-14 CuMo; the superheaters operated at approximately 4800 psi (33.09 MPa) and 1178°F (637°C). Tube wastage was determined by measurements of wall thickness and outside diameter (O.D.) taken before and after service. After 5383 hours, the bare 17-14 CuMo tubing showed a wall thickness wastage of 13 mils (330 μm), while neither the chromized or clad tubing showed any measurable wastage. Macroscopic and microscopic examination of the tubes revealed a pock-marked surface on the bare tubes, while a smooth surface was found on both the chromized and clad tubes. Scale thickness on the bare tubes, the clad tubes, and the chromized tubes was 5.0 to 7.0, 0.4 to 0.8, and 0.4 mils (127 to 178, 0.254 to 0.005, and 0.254 μm) respectively.

Laboratory studies of alkali-iron-trisulfate attack have been undertaken by numerous researchers, among them Rehn [14] and Wolowodiuk, et al. [15] (also discussed in Section 4). Corrosion probes have been installed in utilities around the United States to compare the corrosion rates found in the laboratory tests with actual industrial conditions. Blough has compiled preliminary data from air-cooled retractable corrosion probes at two utility boilers (Gulf Power's

Crist Unit 6 and TVA's Gallatin Unit 2) [16,17]. Alloys tested in the furnace probes are listed in Table 2.

Rings of the test alloys were assembled into a pipe that was placed over a tapered core designed to produce an isothermal temperature. The air-cooled probes are being operated to keep the temperature of all test rings at approximately 1275°F (691°C). At each utility the wall thickness of the probes is being examined ultrasonically every 2000 hours. Detailed coal analysis is also providing corrosion model information of the coal quality variables affecting coal-ash corrosion. After 4000 hours, two of the probes from each utility were destructively examined. Further exposure of probes in each utility will extend to 16,000 hours. Table 3 lists preliminary destructive wall thickness data taken from the 4000-hour probes; the final Electric Power Research Institute report is slated to be released in 1991.

Table 2 Alloys Currently Being Tested in Corrosion Probes in Utility Boilers

Alloy	Cr* (wt%)	Ni* (wt%)	Others* (wt%)
Type 347	17-19	9-13	Cb + Ta 10 x C min.
17-14 CuMo	15.5	14	3.0 Cu, 2.4 Mo
Type 310 Nb	24-26	19-22	---
253 MA	20-22	10-12	1.4-2.0 Si, 0.03-0.08 Ce
FW-4C	20	18	2.4 Si, 2.2 Mn, 2.0 Al
Chromized T-91 (C-E)	8-9.5	---	0.05-1.05 Mo, Chromized Surface
800 HT	19-23	30-35	0.85-1.2 Al + Ti
Tempaloy CR30A	30	55	15 Fe

*Typical analyses for these alloys. All are iron-based alloys except the Tempaloy CR30A, which is a nickel-based alloy.

Table 3 Preliminary Data From Destructive Examinations of Corrosion Probes After 4000 Hours [Metal Temperature 1202°F (650°C)]

Material	Gulf Power--Crist Unit 6 (mil/μm)	TVA--Gallatin Unit 2 (mil/μm)
CR30A	1-2 / 25-50	1-2 / 25-50
Type 310	1-2 / 25-50	1-2 / 25-50
T-91 Chromized	1-2 (26)*/ 25-50 (660)	2-3 / 50-76
Alloy 800	2-5 / 50-127	2-4 (11) / 50-102 (279)
253MA	3-6 (9) / 76-152 (229)	2-3 / 25-76
Type 347	6-9 (14) / 152-229 (356)	2-4 (6) / 50-102 (152)
FW-4C	6-9 / 152-229	2-3 / 25-76
17-14 CuMo	11-33 / 279-838	10 (24) / 254 (610)

*Numbers in parentheses are localized pitting depths.

Section 3

ADVANCES IN UNDERSTANDING OF TRISULFATE ATTACK

Research into molten alkali-iron trisulfate attack in coal combustion atmospheres has been primarily concerned with understanding the effects of various elements on the corrosion resistance of an alloy. The basic mechanisms of attack were well researched in the 1960s and 1970s [18-21]; little research has been directed toward this area in recent years.

Hendry and Lees investigated the properties of alkali-iron trisulfate mixtures and the corrosion behavior of several austenitic steels [22]. With binary diagrams of Na_2SO_4-K_2SO_4, K_2SO_4-$Fe_2(SO_4)_3$, Na_2SO_4-$Fe_2(SO_4)_3$, and $K_3Fe(SO_4)_3$-$Na_3Fe(SO_4)_3$ systems as a starting point, a ternary phase diagram was estimated (Figure 2). The lowest melting-point composition was reasoned to be between the two eutectics, on a line running between $Fe_2(SO_4)_3$ and the minimum of the Na_2SO_4-K_2SO_4 binary. To verify this supposition, the melting points of a series of compositions along lines a/a′ and b/b′ in Figure 2 were determined. A minimum melting temperature occurred at 986°F (530°C) at 14 mol% $Fe_2(SO_4)_3$. Compositions between approximately 6 and 30 mol% $Fe_2(SO_4)_3$ were molten below 1022°F (550°C).

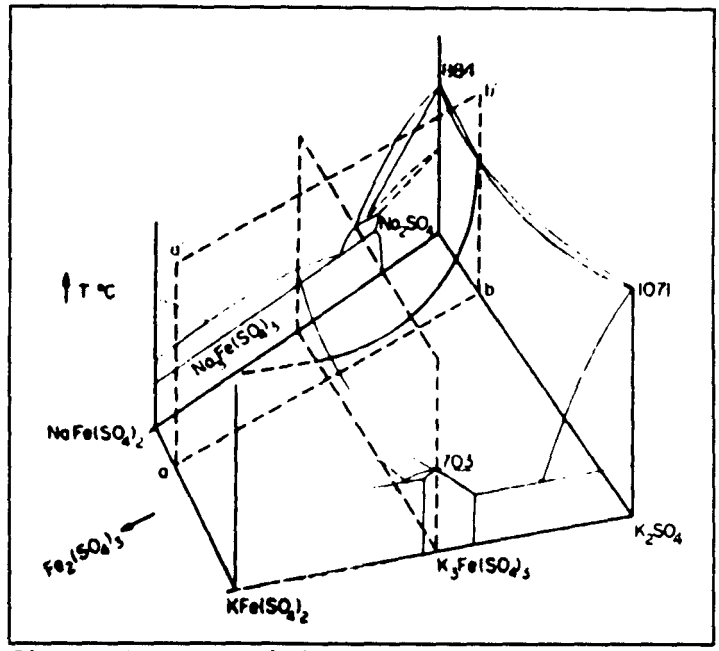

Figure 2 Composition Drawing of Ternary System Na_2SO_4-K_2SO_4-$Fe_2(SO_4)_3$ [21]

A 74 mol% Na_2SO_4 + 20 mol% K_2SO_4 + 6 mol% $Fe_2(SO_4)_3$ composition was selected for detailed analysis. An endothermic reaction and weight loss were observed at 1292°F (700°C) [±68°F (20°C)] under a calculated partial 0.011 psi (76.9 Pa) SO_3 pressure (gas composition 83.7%N_2 + 15%CO_2 + 1%O_2 + 0.3%SO_2). This change was likely due to decomposition of $(Na,K)Fe_2(SO_4)_3$ into Fe_2O_3 and alkali sulfates. Decomposition temperature is determined by the equilibrium of Eq. (1) and thus by the partial pressure of SO_3.

$$Fe_2O_3 + 3SO_3 = Fe_2(SO_4)_3 \quad (1)$$

The range for liquid alkali-iron trisulfates would then be between approximately 1022°F (550°C), where the liquid phase forms, and 1292°F (700°C), where the iron-sulfate solution decomposes.

Weight-gain experiments were conducted on three alloys commonly used in superheaters: Type 316, Type 347, and Esshete 1250. Measurements were taken of weight gain with time on the samples covered with a ternary iron, sodium, potassium sulfate and exposed to the synthetic combustion gases previously examined. Figure 3 shows weight gain curves after normalization and adjustments for the volatilization of alkali sulfates. On the basis of these experiments, the corrosion rates for the alloys tested decrease as follows:

Type 347 < Esshete 1250 < Type 316.

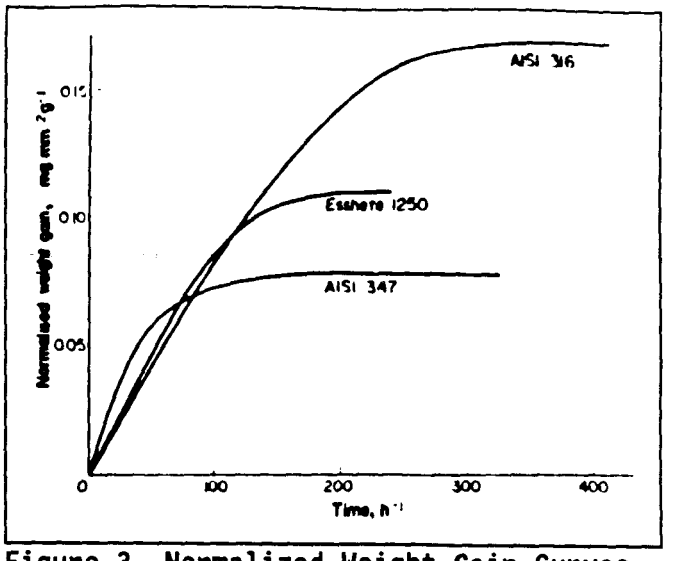

Figure 3 Normalized Weight Gain Curves for Oxidation of Steels in Molten Sulfate Corrected for Volatilization of Alkali Sulfates [22]

From the results of these laboratory trials and data gathered from corrosion probes in actual boilers, a quantitative theory has been developed to explain the dependence of corrosion rate on temperature. A molten sulfate layer has long been known to be the basis for enhanced attack in moderate-temperature salt-induced hot corrosion [1100 to 1400°F (593 to 760°C)]. The thickness of this layer is determined by the temperature of the tube surface at the inner boundary of the sulfate layer, the decomposition temperature of iron sulfate at the outer boundary of the sulfate layer, and the temperature gradient across the molten sulfates. The thickness of this layer can be determined by Eq. (2).

$$X_{melt} = \frac{k_{SO_4}^{2-}\left[T_{decomposition} - \left[\frac{X_{oxide}(q/A)}{k_{oxide}}\right] + T_{metal}\right]}{(q/A)} \qquad (2)$$

where:

X_{melt} = Thickness of molten sulfate layer
X_{oxide} = Thickness of metal oxide layer .
$T_{decomposition}$ = Decomposition temperature of
T_{metal} = Metal surface temperature
$k_{SO_4}^{2-}$ = Thermal conductivity of sulfate layer
k_{oxide} = Thermal conductivity of oxide layer
(q/A) = Heat flux through scale.

A gradient of SO_3 exists between the outer and inner surfaces of the molten layer. The thickness of this layer controls the rate of SO_3 diffusion to the sulfate/oxide interface, as shown in Eq. (3):

$$J_{PSO_3} = \frac{-D\left(P_{SO_3(melt/gas)} - P_{SO_3(melt/oxide)}\right)}{X_{melt}} \qquad (3)$$

where:

D = Diffusivity of SO_3 in molten sulfate

J_{PSO_3} = Flux of SO_3 through molten layer

$P_{SO_3(melt/gas)}$ = Pressure of SO_3 at the outer boundary of the molten layer

$P_{SO_3(melt/oxide)}$ = Pressure of SO_3 at the inner boundary of the molten layer.

As the temperature of the tube surface increases, SO_3 flux also increases, leading to a higher corrosion rate. If the temperature of the tube is increased above the decomposition temperature for iron sulfate, no molten sulfate layer exists, and the corrosion rate drops. An objection to this theory is that it does not explain why corrosion rates of metals in isothermal conditions exhibit the same temperature dependence as cooled tubes in a boiler. If a temperature gradient is driving the corrosion mechanism, experiments carried out isothermally would be expected to show a different temperature dependence and corrosion morphology.

The effect of refractory metals on the resistance of an alloy to alkali-iron trisulfate attack has also been analyzed by Hendry and Lees [22]. Corrosion rates of alloys containing refractory metals have been found to be greater than alloys with the same chromium and nickel content. This behavior is perhaps the result of oxygen gettering by the refractory metals. As the alloy is attacked, refractory metals react with oxygen in the molten sulfates to form stable oxides. Oxygen is consumed from the sulfate melt, shifting the equilibrium of Eq. (4) and leading to higher SO_3 concentrations.

$$SO_4^{2-} = SO_3 + O^{2-} \qquad (4)$$

If the refractory metals do not form a coherent film that protects the metal surface, then the corrosion resistance of an alloy containing refractory metals may be worse than that of an alloy without the refractory metal.

Nanni, et al., examined the attack of pure iron, manganese, and chromium in a $3.6\%O_2$-$0.25\%SO_2$ gas stream between 1112 and 1472°F (600 and 800°C) [22]. Isolated areas of both iron and manganese suffered alkali-iron trisulfate attack, while chromium showed no evidence of attack. Generalized oxidation and sulfidation of the specimens were observed in addition to hot corrosion. The morphology of corrosion on iron samples exhibits a layered structure comprised of an outer layer of Fe_2O_3, Fe_3O_4 mixed with FeO, and an inner layer of FeS in FeO. Manganese showed a similar structure with layers of Mn_3O_4, MnO, and MnO mixed with MnS. Chromium showed only a thin film of Cr_2O_3.

Gesmundo and Viani [24] reviewed the results from Nanni's investigations. To form a liquid phase at the temperature where alkali-iron trisulfate attack occurs, sodium sulfate must form a low-melting-point solution with another species. As Figure 4 shows, two species of iron sulfate could form a solution with sodium sulfate: trivalent iron sulfate and divalent iron sulfate. Trivalent iron sulfate forms in the presence of hematite [Eq. (5)], while divalent iron sulfate may form from hematite or magnetite by Eqs. (6) and (7).

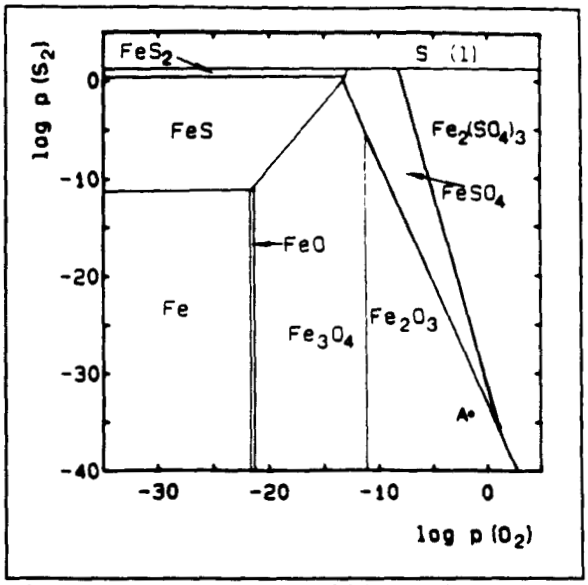

Figure 4 Phase Stability Diagram of Fe-O-S at 1292°F (700°C)--Point A Corresponds to the Equilibrium Gas Composition

$$Fe_2O_3 + 3SO_3 = 2Fe(SO_4)_{1.5} \quad (5)$$

$$Fe_2O_3 + 2SO_3 = 2FeSO_4 + 1/2O_2 \quad (6)$$

$$Fe_3O_4 + 3SO_3 = 3FeSO_4 + 1/2O_2 \quad (7)$$

Manganese, like iron, can form both divalent and trivalent sulfates. The stability diagram for the manganese-oxygen-sulfur system indicates that divalent manganese in manganese sulfate is the form stable in the presence of manganese oxides. At 1112 and 1292°F (600 and 700°C) in $3.6\%O_2$-$0.25\%SO_2$, divalent manganese sulfate is the stable species.

The reaction mechanisms and transport of iron from the metal surface through the inner oxide layer to the molten sulfate may occur in the following manner: Iron oxides contain metal vacancies as the prevailing lattice defect. Oxide growth is primarily by outward migration of metal ions. During low-temperature hot corrosion, iron ions migrate from the metal surface through the oxide to the molten sulfate. Several reactions may take place at this interface. The iron may combine with dissolved oxygen or with SO_3, as shown in Eqs. (8) and (9).

$$Fe + 1/2O_2 = FeO \quad (8)$$

$$Fe + SO_3 = FeO + SO_2 \quad (9)$$

Sulfur trioxide is available at the interface by diffusion of either SO_3 or $S_2O_7^{2-}$ through the molten sulfate or by the decomposition of Na_2SO_4, as illustrated in Eq. (10):

$$Na_2SO_4 = Na_2O + SO_3 \quad (10)$$

Sulfate ions may also react directly with the iron. A coupled set of reactions at the inner and outer interfaces of the molten layer is illustrated in Eqs. (11) and (12).

$$Fe + SO_4^{2-} = FeO + SO_3^{2-} \quad (11)$$

$$SO_3^{2-} + 1/2O_2 = SO_4^{2-} \quad (12)$$

In competition with the oxide formation reactions given in Eqs. (11) and (12), iron oxide may be converted into $FeSO_4$, which dissolves into the molten sulfate layer:

$$FeO + SO_3 = FeSO_4 \quad (13)$$

As the sulfate solution saturates with $FeSO_4$, iron oxides may be precipitated from the molten sulfate in regions of high oxygen activity. Reprecipitation of oxide islands in the liquid sulfate creates an outer layer of porous, unprotective scale. Local oxide precipitation allows alkali sulfates to continue to dissolve more of the inner oxide layer than without saturation of the sulfate solution. A cycle of oxide dissolution and reprecipitation may continue until the porous oxides disperse and absorb the alkali sulfates. In a boiler, a continuous influx of alkali sulfates allows the attack to continue indefinitely.

Low-temperature hot corrosion of nickel under a coating of sodium sulfate was studied by Lillerud and Kofstad [24]. Nickel coated with sodium sulfate was exposed to O_2 + 4%SO_2 atmospheres at 1220 and 1652°F (660 and 900°C). Weight gains as a function of time for nickel exposed to O_2 + 4%SO_2 with and without a sodium sulfate coating are shown in Figures 5 and 6. Weight gain was slower for the sample coated with sodium sulfate at 1220°F (660°C). No molten phases are present at this temperature. The sodium sulfate coating forms a protective barrier on the nickel surface. Both coated and uncoated specimens formed a scale consisting of NiO and Ni_3S_2.

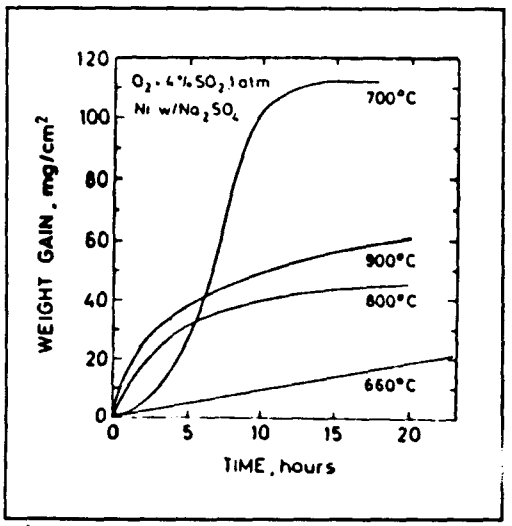

Figure 5 Reaction of Nickel with Na_2SO_4 Layer (2.5 mg/cm²) With 1 atm O_2 + 4% SO_2 at 1220 to 1652°F (660 to 900°C) [25]

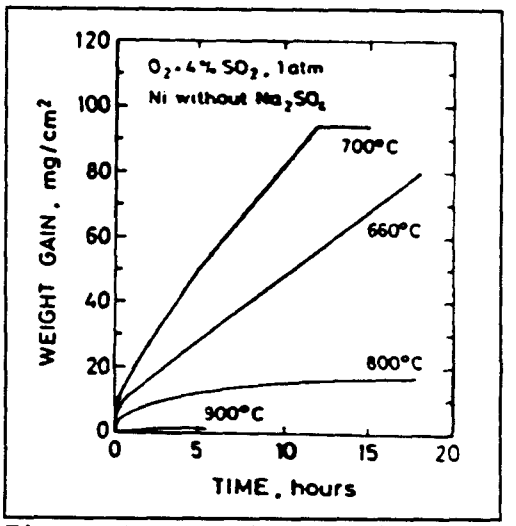

Figure 6 Reaction of Nickel With 1 atm O_2 + 4% SO_2 at 1220 to 1652°F (660 to 900°C) [25]

At 1292 and 1472°F (700 and 800°C), a temperature where liquid Na_2SO_4 + $NiSO_4$ can form, coated specimens suffered increased corrosion rates. The eutectic temperature for the Na_2SO_4-$NiSO_4$ system is 1240°F (671°C). Reaction kinetics for the coated specimens at 1292°F (700°C) showed an induction period of 3 to 4 hours, then a much greater rate of weight gain than the uncoated specimen. Samples of the coating showed increasing nickel concentration during the induction period, until a mole fraction of 0.26 $NiSO_4$ was reached, when molten sulfates formed. Specimens with a liquid phase displayed a scale morphology of $Na_2Ni(SO_4)_2$ surrounding islands of NiO.

In a set of experiments conducted at 1292°F (700°C), specimens were reacted under different pressures of O_2 + 4%SO_2. Decreasing pressures led to longer induction times; molten sulfate formed on thicker oxide scales, and the overall effects of a molten layer were reduced. Below 0.01 atm, no molten sulfate was detected.

Between 1240°F (671°C)--the liquidous point of the Na_2SO_4-$NiSO_4$ eutectic, and 1623°F (884°C)--where pure Na_2SO_4 melts, sodium sulfate attack on nickel may start in the following way: Initially, a solid layer of sodium sulfate covers a nickel surface. Oxygen and sulfur oxides penetrate the sulfate coating to form nickel oxides and sulfides on the metal surface. NiO reacts with SO_3 to form $NiSO_4$, which forms a solid and then liquid solution with Na_2SO_4. A three-layered morphology develops:

- An outer layer consisting of Ni + $(Na_2SO_4 + NiSO_4)_{liq}$.
- Beneath this, a region consisting of NiO and Ni_3S_2
- Next to the metal, a sulfur-enriched region where the sulfide at temperature is present as $(Ni\text{-}S)_{liq}$.

Nickel diffuses through the sulfide phase to the outer layer, while O_2 and SO_3 diffuse inward through the liquid sulfate. At the boundary between the liquid and sulfide/oxide layer, nickel and $NiSO_4$ react to form NiO and Ni_3S_2 by Eqs. (14) and (15).

$$4Ni + NiSO_4 = 4NiO + [NiS] \quad (14)$$

$$Ni + [NiS] = Ni_3S_2 \quad (15)$$

As a result of the higher partial pressure of SO_3 at lower temperatures [1292°F (700°C)], SO_3 diffusing through the sulfate greatly outweighs the effect of oxygen transport. The exact transporting species through the molten layer is not known. Possible species include the pyrosulfate ion ($S_2O_7^{2-}$), nickel sulfate ($NiSO_4$), or several ionic sulfur oxides.

Section 4

ALLOY DEVELOPMENT AND CHARACTERIZATION

New materials developments in the last decade have been driven by increasingly severe operating requirements and higher materials cost. New steels for high-temperature service and various types of coextruded tube have been introduced within the last decade. The push for greater thermal efficiency has raised both steam and flue gas temperatures, while rising fuel costs have led to the use of coals high in sulfur and salts. The combustion environment is almost optimum for corrosion by the alkali-iron trisulfate mechanism. Rising costs of the materials for alloying steel and the need for both corrosion resistance and high temperature strength have prompted the development of claddings, coatings, and coextruded tubes.

A multifaceted fireside corrosion testing program was carried out by Rehn during an EPRI project [14]. Characterization of commercial steels, experimental alloys, diffusion and plasma spray-coated materials was carried out by repeated cycling of coupons in a simulated coal combustion atmosphere. Tables 4 and 5 list the alloys and coatings investigated during the project.

Testing was carried out in sealed retorts heated to 675°C (1250°F) for 48 hours. The samples were coated with a synthetic ash of composed of $37.5\%Na_2SO_4$-$37.5\%K_2SO_4$-$25\%Fe_2O_3$. A synthetic flue gas ($72\%N_2$-$14\%CO_2$-$10\%H_2O$-$3.6\%O_2$-$0.25\%SO_2$) was passed over the samples.

Results of the alloys repeatedly cycled through 48-hour corrosion exposure, with and without descaling between exposures, are shown in Figures 7 through 9. Average losses for each exposure are listed in Table 6. There were two types of experimental alloys: modifications of Type 347 and modifications of Alloy 4--a composition found particularly corrosion resistant in a previous project [10]. Alloys in the "four" series, along with 7M, 7C, and 7B, with commercial alloys Sandvick 253 MA and Nitronic 60 show the beneficial effects of silicon, manganese, and rare earth additions to the base alloy. Nitronic 60 proved to be the most resistant commercial alloy tested, showing one-fifth the loss of Type 304 stainless steel. Alloys in the "four" series produced extremely tenacious scales, which required harsh measures to remove.

To study the effects of chemical concentration gradients on the corrosion resistance of various alloys, alloys were coupled by welding one alloy onto another, rolling these couples into sheets, and cutting them into coupons. Results after repeated exposures were inconclusive, no clear cases of galvanic attack were detected on any specimens.

Table 7 lists the performance of coatings under repeated testing cycles. The coatings tested all gave good performance for the first several cycles, until the coating either spalled or wore through. Alonized steels performed well for three cycles, until the aluminum-rich layer was pitted through. After loss of the alonized layer, corrosion resistance was that of the base metal. Plasma-sprayed coatings protected the base metal as long as the coating did not spall or peel. Magnesium zirconate proved to be completely resistant to corrosive attack; however, the thick coatings [20 - 25 mil (508 - 635 μm)] applied to an austenitic steel spalled as a result of differences in the expansion coefficient. Thin coatings [10 mil (254 μm)] coatings or coatings on ferritic steels did not spall.

Table 4 Commercial Steels and Alloys Studied During EPRI's Fireside Corrosion Project [14]

Alloy	Chemical Composition (wt%)							
	Cr	Ni	Si	Mn	Al	C	Fe	Other
Commercial:								
AISI 304	18.5	9.0	0.7	1.1	---	0.06	Bal	---
AISI 347	19.0	11.5	0.5	1.0	---	0.06	Bal	0.80Cb
AISI 309	22.0	14.7	0.7	1.85	---	0.059	Bal	---
AISI 310	25.0	20.4	0.5	1.8	---	0.07	Bal	---
Sandvik 253 MA	21.0	11.0	1.8	0.3	---	0.10	Bal	0.16 N, 0.03 Ce
Carpenter 10	15.8	17.7	0.51	0.77	---	0.03	Bal	0.035 N, 0.19 Cu, 0.27 Mo
Nitronic 60	16.4	8.3	3.8	8.15	---	0.09	Bal	0.12 N
Incoloy 800H	20.4	31.2	0.24	0.88	0.47	0.0565	Bal	0.46 Ti, 0.6 Cu
AISI 312 (weld deposit)	29.6	7.14	0.3	1.4	---	0.13	Bal	---
Special:								
7M	20.3	11.7	2.0	2.4	---	0.05	Bal	2.47 Cb
7B	19.8	12.4	1.9	3.1	---	0.047	Bal	2.1 Cb
7C	20.3	12.4	2.1	7.1	---	0.038	Bal	1.6 Cb
4	20.0	24.1	2.4	0.45	2.1	0.02	Bal	---
4A	21.0	19.7	2.3	0.36	2.1	0.10	Bal	---
4B	20.0	17.7	2.4	0.5	2.1	0.02	Bal	---
4C	20.0	17.8	2.4	2.2	2.3	0.012	Bal	---
4D	20.7	15.2	2.4	9.5	2.4	0.025	Bal	---
4E	19.4	14.8	2.6	9.6	---	0.029	Bal	4.2 Zr

Gradient Test:	Sheet Alloy (wt%)				Weld Filler Metal (wt%)			
	Cr	Ni	Mn	Si	Cr	Ni	Mn	Si
16 Cr-25	16.0	18.0	1.0	0.5	25.0	20.0	1.8	0.5
25 Cr-30	25.0	20.0	1.8	0.5	30.0	18.0	1.0	0.5
25 Cr-18	25.0	20.0	1.8	0.5	8.0	12.0	1.0	0.5
19 Ni-13	25.0	19.0	1.0	1.0	22.0	13.0	2.0	1.0
12 Ni-20	22.0	12.5	1.0	1.0	25.0	20.0	1.8	0.5
20 Ni-8	25.0	20.0	1.8	0.5	30.0	8.0	1.0	0.5

Table 5 Coatings Studied During EPRI's Fireside Corrosion Project [14]

Surface Alloy Treatments

Type	Substrate Alloy	Coating Process	Thickness, μm (in.)
Alonized	Incoloy 800	Commercial--Furnace at 1010°C (1850°F)	127 - 203 (0.005 - 0.008)
Alonized	Type 310SS	Commercial--Furnace at 1010°C (1850°F)	76 - 127 (0.003 - 0.005)
Chromized	Type 304SS	Commercial--Furnace at 1038°C (1900°F)	25 - 51 (0.001 - 0.002) (Above 40%Cr)

Plasma Spray Coatings

Type	Substrate Alloy	Base Alloy	Thickness, μm (in.)
Magnesium Zirconate (Metco 210)	Type 304SS	Ni-Al	254-280 (0.010 - 0.011)
Magnesium Zirconate (Metco 210)	2-1/4%Cr-1%Mo-2%Ni Ferritic Steel	Ni-Cr-Al	559 ±76 (0.022 ±0.003)
Magnesium Zirconate (Metco 210)	Type 347SS	Ni-Cr-Al	559 ±76 (0.022 ±0.003)
Kanthal	Type 309SS	Fe-25%Cr-5%Al (Prealloyed)	51 - 102 (0.002 - 0.004)
Fe-Cr-Al (Elemental)	Ferritic HT-9	Fe-18%Cr-10%Al (From Fe-Cr alloy and Al powders)	127 - 203 (0.005 - 0.008)
Ni-Al (Metco 404)	Type 347SS	80%Ni-20%Al	254 ±25 (0.010 ±0.001)
Ni-Cr-Al-Fe-Mo (Metco 444)	Ferritic 2-1/4%Cr-1%Mo-2% Ni	Ni-14%Cr-7%Al-6%Mo-5%Fe	508 - 635 (0.020 - 0.025)
Ni-Cr-Al-Fe-Mo (Metco 444)	Type 304SS	Ni-14%Cr-7%Al-6%Mo-5%Fe	508 - 635 (0.020 - 0.025)

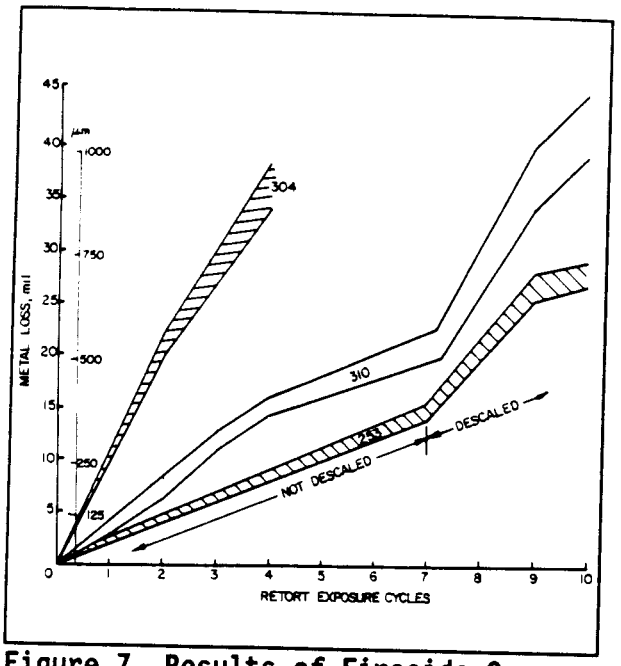

Figure 7 Results of Fireside Corrosion of Commercial Alloys

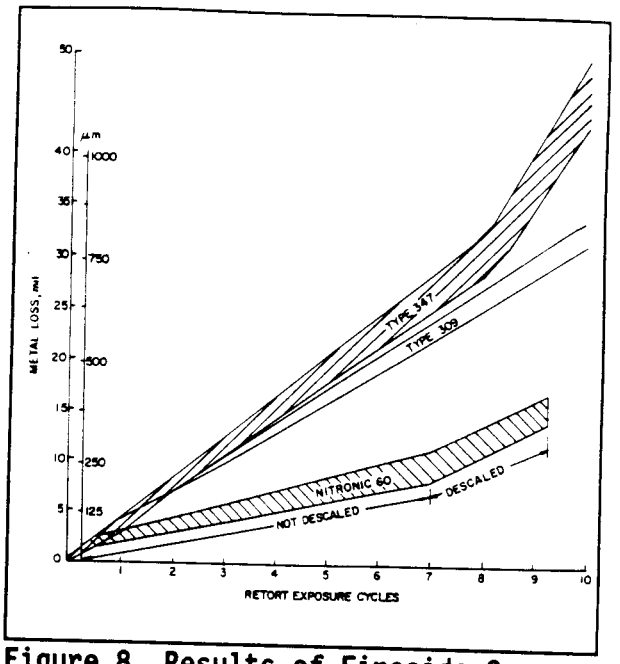

Figure 8 Results of Fireside Corrosion of Commercial Stainless Steel

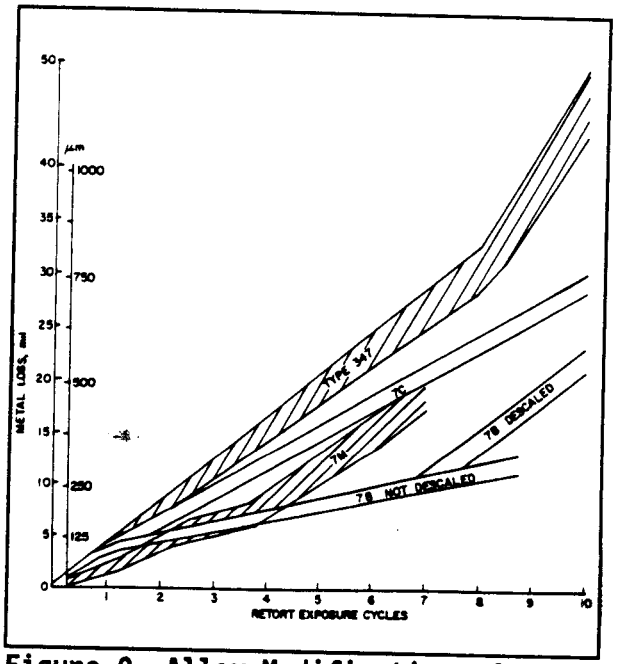

Figure 9 Alloy Modification of Type 347 for Fireside Corrosion Test Cycles

Table 6 Average Corrosion Losses After 48-Hour Exposure

Alloy	Average Corrosion Loss mil	Average Corrosion Loss μm
AISI 304	9.0	229
AISI 347	4.5	114
AISI 310	5.0-6.0	127-152
Sandvik 253 MA	2.5	64
Nitronic 60	1.75	44
7M	4.3-4.9	109-124
7C	4.3-4.9	109-124
7B	1.4-2.4	36-61
4	1.2	30
4B	1.0	25
4C	0.9	20-23
4D	0.6-0.8	15-20
4E	1.7	43

Table 7 Performance of Coatings After Repeated Cycles

Coating/Base Metal	Length of Protection (Failure Mode)
Alonized 800 stainless	3 cycles (corrosion)
Alonized 310 stainless	3 cycles (corrosion)
Magnesium Zirconate	
Thin coating	10+ cycles
Thick coating/ferritic steel	8+ cycles
Thick coating/austenitic steel	3+ cycles (spalling)
Nickel Aluminide	
Kanthal	3 cycles (spalling)
Metco 404	9+ cycles
Metco 444 austenitic steel	7+ cycles
Metco 444 ferritic steel	3+ cycles

Kihara, et al., characterized the corrosion properties of Type 347H and 17-14 CuMo stainless steels [26]. Tests were conducted using synthetic coal ashes and flue gases. The effects of different compositions of synthetic coal ash, catalysis, preheating of samples, sulfur dioxide content, temperature, ash volume, temperature gradient, and various inhibitors were studied. Type 347H had greater corrosion resistance than 17-14 CuMo under all conditions. The difference in corrosion rates was attributed to the detrimental effect of molybdenum in the 17-14 CuMo and the beneficial effect of Nb in the Type 347H. Molybdenum may flux into the molten sulfate, increasing its acidity. The consequences of molybdenum in a sulfate were demonstrated by progressive additions of MoO_3 to a $50\%Na_2SO_4$-$50\%K_2SO_4$ synthetic coal ash, as shown in Figure 10.

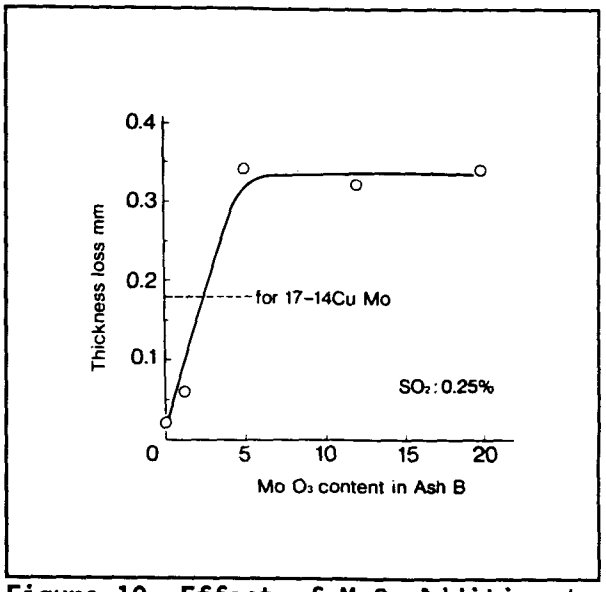

Figure 10 Effect of MoO_3 Addition to Ash B on Corrosion Loss of 347H at 700°C for 25 Hours in 0.25%SO_2 Flue Gas

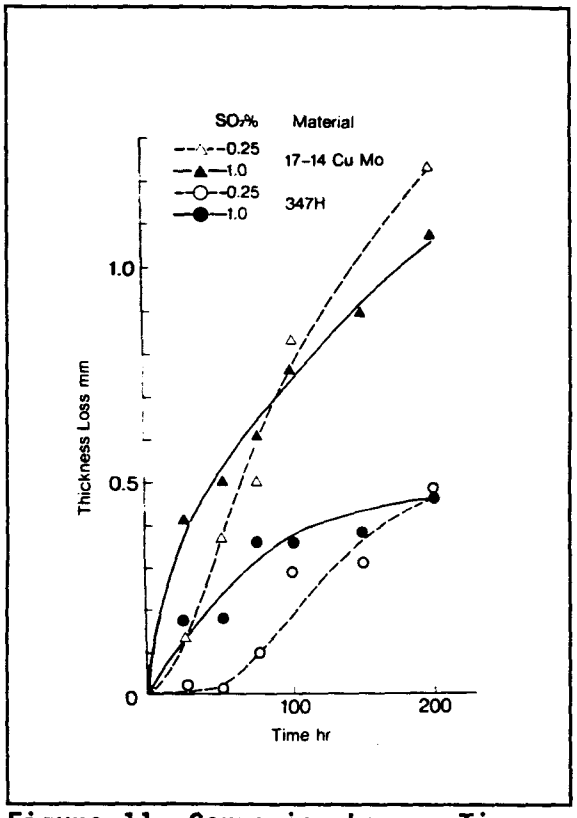

Figure 11 Corrosion Loss - Time Curves for 17-14 CuMo and 347H at 700°C in Ash B as a Function of SO_2 Content of Flue Gas

For the first 50 hours, corrosion rates for Type 347H were very low at 1292°F (700°C) in a 0.25% SO_2 flue gas, then quickly accelerated (Figure 11). This initial incubation period was attributed to a slow rate of formation of alkali-iron-trisulfate on the metal surface. When the SO_2 level was increased, or the SO_2 was catalyzed to SO_3, the incubation period disappeared.

Five different compositions of synthetic coal ash were used to study the effect of ash composition on the corrosion rate and mechanism. Table 8 lists the ash composition and corrosion losses during a test conducted at 1292°F (700°C) in 0.3% SO_2 for 50 hours. Ash E had a composition simulating deposits found on test probes. The corrosion rate of 17-14 CuMo in a boiler test probe installed for 10,000 hours was 27.6 mil/yr (700 μm/yr). Ash E gave results close to those found in the field.

Tamura, et al., studied the hot corrosion resistance of alloys from the Cr-Fe-Ni system, along with the alloying effects of minor additions of various elements [27,28]. They characterized hot corrosion susceptibility was by weight

Table 8 Ash Composition and Corrosion Losses During Testing at 1292°F (700°C)

Ash	Ash Composition (mol%)		Corrosion Rate mils/yr	mm/yr
A	Na_2SO_4	(37.5)	984	25.0
	K_2SO_4	(37.5)		
	Fe_2O_3	(25.0)		
B	Na_2SO_4	(50.0)	1319	33.5
	K_2SO_4	(50.0)		
C	$LiSO_4$	(33.3)	1299	33.0
	Na_2SO_4	(33.3)		
	K_2SO_4	(33.3)		
D	Na_2SO_4	(74.0)	1063	27.0
	K_2SO_4	(20.0)		
	$Fe_2(SO_4)3$	(6.0)		
E	SiO_2	(17.4)	59	1.5
	Al_2O_3	(9.7)		
	Fe_2O_3	(26.3)		
	$CaSO_4$	(18.6)		
	K_2SO_4	(1.3)		
	Na_2SO_4	(6.0)		

loss measurements in tests conducted at 1292°F (700°C) for 100 hours [27]. Coupons were exposed to a synthetic coal ash of 30%Na_2SO4-41%K_2SO_4-25%Fe_2O_3 and a gas mixture containing 1%SO_2. Weight loss data for the alloys examined are listed in Table 9.

As shown in Figure 12, a rise in the chromium content in an alloy increased its corrosion resistance until the chromium content reached 35 wt%, where no further benefit was produced. Additions of iron up to 25 wt%, improved corrosion resistance up to 25 wt%; above 25 wt%, iron, the corrosion resistance of the alloy, decreased, as shown in Figure 13. The limited data available seems to indicate that nickel-based alloys are more resistant to hot corrosion under these conditions than cobalt-based alloys with the same iron and chromium content. Of the alloys examined, a 35%Cr-45%Ni-20%Fe alloy exhibited the greatest corrosion resistance.

Table 9 Results of Coal Ash Corrosion Test on Cr-Ni-Fe Ternary Alloys

Alloy	Symbol	Chemical composition (wt%)								Weight loss (mg/cm²) (700°C, 100h)
		C	Si	Mn	P	S	Ni	Cr	Fe	
20%Cr	CR20A	005	tr	tr	0033	-	bal.	20.61	16.63	94
30%Cr	CR30A	005	tr	tr	0025	-	bal.	29.62	15.32	34
	CR30B	005	60	60	0120	-	13.49	29.19	bal.	82
35%Cr	CR35B	050	tr	tr	tr	0006	bal.	35.31	tr	21
	CR35C	020	tr	tr	tr	0005	bal.	34.23	11.00	18
	CR35D	007	tr	tr	0029	-	bal.	34.99	22.70	11
	CR35E	005	57	34	0110	-	15.16	34.57	bal.	49
40%Cr	CR40A	016	01	tr	0070	0012	bal.	40.69	tr	21
	CR40B	009	05	tr	0057	0011	bal.	40.75	3.73	14
	CR40C	020	04	tr	0056	0006	bal.	38.79	9.45	19
	CR40D	003	tr	tr	0025	-	bal.	38.97	19.41	11
	CR40E	005	01	tr	0029	-	bal.	39.68	22.66	13
	CR40F	005	86	-	-	-	bal.	39.36	29.60	29
	CR40G	005	90	-	-	-	bal.	39.32	37.42	32
	CR40H	005	61	56	0110	-	16.78	38.85	bal.	30
45%Cr	CR45A	010	tr	tr	tr	0006	bal.	46.02	11.14	21
	CR45B	005	56	-	0110	-	21.90	43.54	bal.	31
50%Cr	CR50A	020	tr	01	tr.	-	bal.	50.49	tr.	11
	CR50B	050	60	58	0430	-	25.28	47.74	bal.	36
60%Cr	CR60A	050	55	54	0091	-	28.01	57.28	bal.	24
• Co base	CR35 Co	010	02	tr	tr.	-	tr.	35.00	tr.	26
	CR40 Co	020	02	tr.	0036	-	tr.	38.80	8.80	44

— not analyzed • balance is Co.

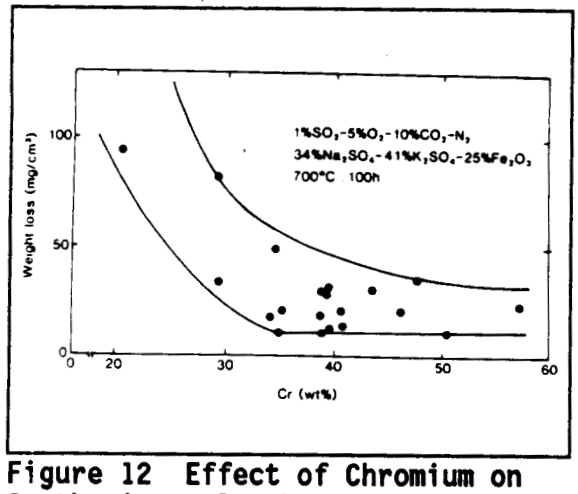

Figure 12 Effect of Chromium on Synthetic Coal-Ash Corrosion Loss of Ni-Cr-Fe Alloys at 1292°F (700°C) for 100 Hours

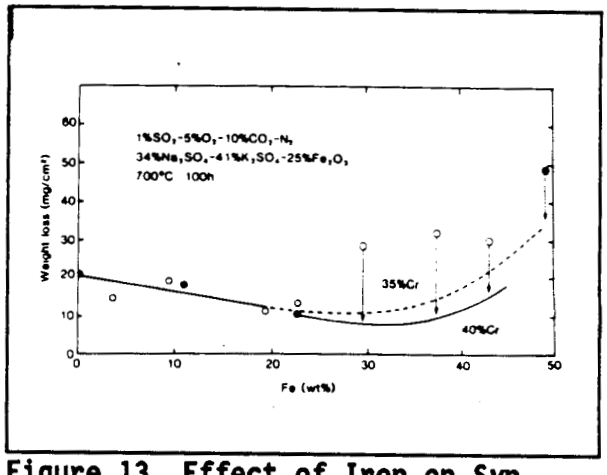

Figure 13 Effect of Iron on Synthetic Coal-Ash Corrosion Loss of 34 or 40 Cr-Ni-Fe Alloys at 1292°F (700°C) for 100 Hours

The 35%Cr-45%Ni-20%Fe alloy was modified with small additions of several elements to determine the effects of the modification on coal-ash corrosion resistance. In every case, the parent alloy had better corrosion resistance than the modified alloys, as illustrated in Table 10. These results contradict those of Rehn, who found that silicon, aluminum, niobium, and titanium were beneficial alloying elements for coal-ash corrosion resistance [14].

Table 10 Weight Loss Data for Tests at 1292°F (700°C) for 100 Hours [27]

Symbol	Chemical composition (wt%)									Weight loss (mg/cm²) (700°C, 100h)
	C	Si	Mn	P	S	Ni	Cr	Fe	alloying element	
CR35F	.05	tr.	tr.	tr.	tr.	bal.	35.31	tr.	-	20
CR35G	.02	tr.	tr.	tr.	tr.	bal.	33.97	tr.	0.5Nb	30
CR35H	.04	.45	.03	.0029	.0052	44.22	33.16	bal.	0.24Ti	12
CR35I	.01	.42	.03	.0025	.0056	44.43	32.93	bal.	0.59Ti	19
CR35J	.02	.40	.03	.0033	.0078	43.24	33.70	bal.	0.98Ti	39
CR35K	.03	.37	.06	.0104	.0051	45.29	34.39	bal.	0.65Mo	22
CR35L	.03	.35	.05	.0081	.0056	45.38	34.81	bal.	1.72Mo	34
CR35M	.02	.27	.04	.0036	.0062	46.49	35.72	bal.	3.94Mo	45
CR35N	.03	.39	.04	.0095	.0045	48.51	33.54	bal.	0.88Al	20
CR35O	.03	.38	.06	.0078	.0036	47.61	32.58	bal.	1.90Al	29
CR35P	.03	.35	.05	.0074	.0020	47.90	32.23	bal.	5.25Al	41
CR35D	.007	tr.	tr.	.0029	tr.	bal.	34.99	22.70	-	11
CR35Q	.006	.28	tr.	.0025	tr.	bal.	34.88	22.71	Si	18

The Tamura studies showed that an alloy consisting of 0.06%C-35%Cr-45%Ni-0.5%Nb-Fe, designated CR35A, had excellent corrosion resistance, good mechanical properties, and good weldability. The coal-ash corrosion resistance of Alloy CR35A and several commercial alloys is shown in Figure 14.

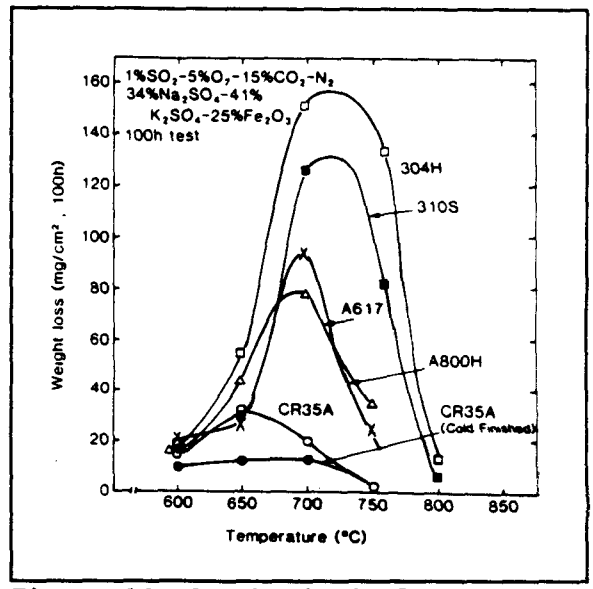

Figure 14 Synthetic Coal-Ash Corrosion of Alloy CR35A and Commercial Alloys. Surface Cold Finishing on Alloy CR35A Further Reduced the Corrosion Loss.

Table 11 lists the alloys tested by Tamura, et al. [28]. Corrosive conditions were produced by a 34%Na_2SO_4-41%K_2SO_4-25%Fe_2SO_4 artificial coal ash in an atmosphere containing either 0.2% or 1% SO_2 in a 5%O_2-15%CO_2-N_2. Tests conducted at 1200°F (650°C) in 0.2%SO_2 are shown in Figure 15. The modified alloys (A-1 and A-2) performed as well in this test as Type 300 series stainless steels with higher chromium and nickel contents. A much harsher environment existed in the 1.0% SO_2 atmosphere at 1292°F (700°C); corrosive losses are shown in Figure 16. High-chromium alloys exhibited greater corrosion resistance than alloys with a lower chromium content. The CR35A modified stainless steels exhibited corrosion resistance better than similar Type 300 series stainless steels.

Table 11 Chemical Composition of Alloy for Corrosion Tests (wt%)

Alloy	C	Si	Mn	Ni	Cr	Mo	Nb	Al	Ti	Fe	Others
Type 304H	0.06	0.63	1.61	8.75	18.22	—	—	—	—	bal.	
Type 316H	0.06	0.65	1.63	11.75	16.36	2.24	—	—	—	bal.	
Type 321H	0.06	0.44	1.54	10.72	17.47	—	—	—	0.39	bal.	
Type 347H	0.07	0.61	1.64	11.99	18.03	—	0.69	—	—	bal.	
Type 310S	0.06	0.68	1.67	20.84	24.40	—	—	—	—	bal.	
Type 314	0.10	2.33	1.52	19.58	24.27	—	—	—	—	bal.	
17-14CuMo	0.12	0.56	0.77	14.46	15.44	2.42	0.43	—	0.23	bal.	2.97Cu
Alloy 800H	0.07	0.57	0.90	31.91	21.16	—	—	0.49	0.50	bal.	
Alloy 807	0.09	0.69	0.93	39.13	21.06	—	1.19	0.27	0.48	bal.	8.12Co 4.61W
Alloy 617	0.06	0.16	0.03	bal.	22.92	9.20	—	0.85	0.48	0.52	11.55Co
Alloy 671	0.06	0.10	0.01	bal.	49.01	—	—	—	0.25	—	
Alloy 690	0.01	0.21	0.35	bal.	29.43	—	—	—	—	10.51	
TEMPALOY F-9	0.06	0.41	0.61	—	9.26	1.08	0.23	—	—	bal.	0.21V
TEMPALOY A-1	0.09	0.49	1.58	10.77	17.97	—	0.15	—	0.07	bal.	
TEMPALOY A-2	0.09	0.50	1.50	14.05	18.12	1.57	0.23	—	0.16	bal.	0.003B
TEMPALOY CR30A	0.06	0.27	0.20	50.99	30.52	2.11	—	0.14	0.18	bal.	
NAC CR35A	0.07	0.07	0.01	46.15	35.04	—	0.52	—	—	bal.	

—: Not analyzed.
TEMPALOY and NAC are registered trademarks of NKK.

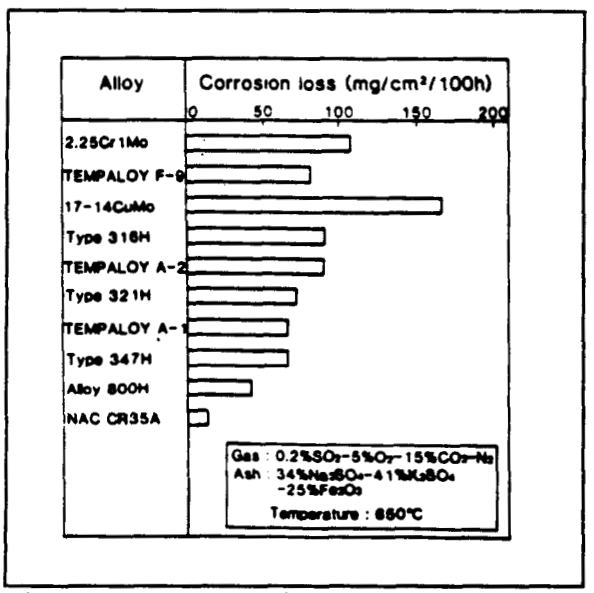

Figure 15 Corrosion Rate in Coal Ash Corrosion Test for Various Alloys [1200°F (650°C), 100-h]

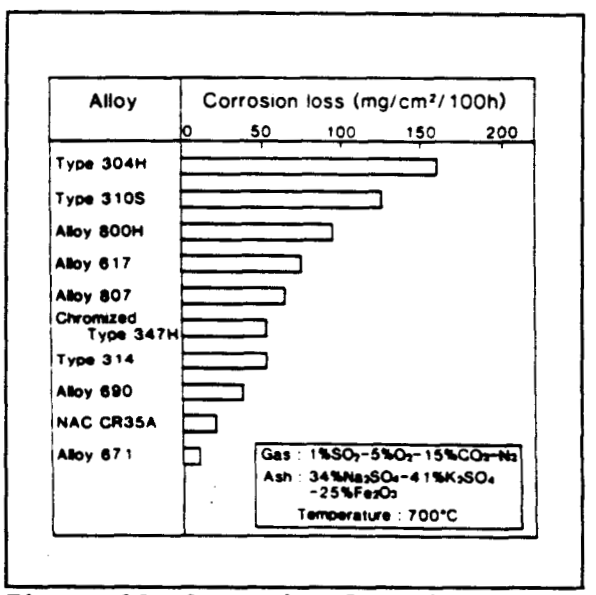

Figure 16 Corrosion Rate in Coal Ash Corrosion Tests for Various Cladding Alloys and Nickel-Based Alloys [1292°F (700°C), 100-h]

Nakagawa, et al., investigated the hot-corrosion resistance of chromized Type 347H and 17-14 CuMo steels by electrochemical means and by weight-loss measurements [29]. Chromized and untreated samples were coated with differing synthetic ash mixtures and exposed to environments containing varying quantities of SO_2 at 1200°F (650°C). Chromized samples exhibited much lower losses over the entire range of SO_2 concentrations and ash compositions than the samples without chromizing. Corrosion which did occur on the chromized samples took the form of pits. The length of time to the initiation of pitting seemed a function of ash composition and SO_2 concentration.

Potentiodynamic and potentiostatic polarization measurements of chromized and unchromized Type 347H and 17-14 CuMo steels were conducted to determine the nature of the corrosion processes. Chromized specimens exhibited lower anodic current densities than unchromized specimens over the entire range examined, which was attributed to a Cr_2O_3 barrier at the interface. Pitting was observed at certain "breakthrough" potentials, with an abrupt increase in anodic current density. Hysterisis loops were observed in reversed potentiodynamic sweeps after pits had formed, suggesting that no repassivation of the pits occurred.

Nakagawa, et al., evaluated several superheater materials by electrochemical polarization [30]. Potentiodynamic anodic polarization and free corrosion potential measurements were conducted in a ternary eutectic of lithium, sodium and potassium sulfates at 1200°F (650°C). Experiments were conducted under three different atmospheres: air and synthetic flue gases containing either 0.25% or 1.0% SO_2. All alloys exhibited passivation in air to some degree. Passivity lasted during anodic polarization until a "breakthrough" potential was reached. Additions of sulfur dioxide reduced the passive plateau for all alloys; the breakthrough potential was not changed. The breakthrough potentials increased in the following order:

Type 310 > Type 347 > 17-14 CuMo

Corrosion of two low-chromium steels, T-22 and HT91, by sodium sulfate between 1112 and 1472°F (600°C and 800°C) was investigated by Gesmundo and Nanni [31]. Measurements of weight loss with time for both steels are shown in Figures 17 and 18. The T-22 steel did not show the bell-shaped dependence of corrosion rate on temperature that the higher-chromium alloys would; instead, the corrosion rate increased almost linearly with temperature. This behavior may have been the result of the high rate of oxidation at the higher temperatures, which masked any decrease in hot corrosion.

Corrosion of Ni-30%Cr and Co-30%Cr alloys in sodium sulfate was investigated by Luthra and Shores [32]. Weight gain rates, shown in Figures 19 and 20, were measured between 1112 and 1652°F (600 and 900°C). Peak corrosion rates for the nickel-based alloy occurred between 1292 and 1382°F (700 and 750°C), while the cobalt-based alloy suffered the greatest corrosion between 1200 and 1292°F (650 and 700°C). Although pitting was observed on the cobalt-based alloy, the nickel-based alloy underwent uniform corrosion over its entire surface. To determine the corroding species, the corrosion deposits from both alloys were analyzed for water soluble salts. Chromium salts existed in concentrations less than 5 micrograms/cm^2 of sample for both the nickel- and cobalt-based alloys, while the concentration of nickel or cobalt salts changed in the same proportion as the weight gain.

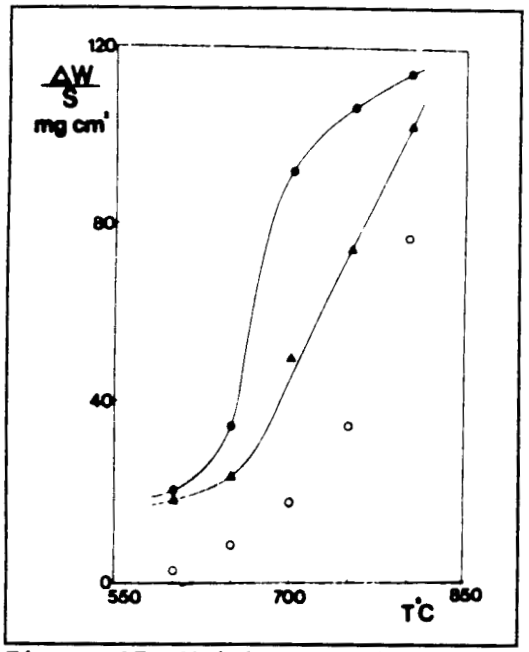

Figure 17 Weight Loss Per Unit Area vs. Temperature (A213 T-22)

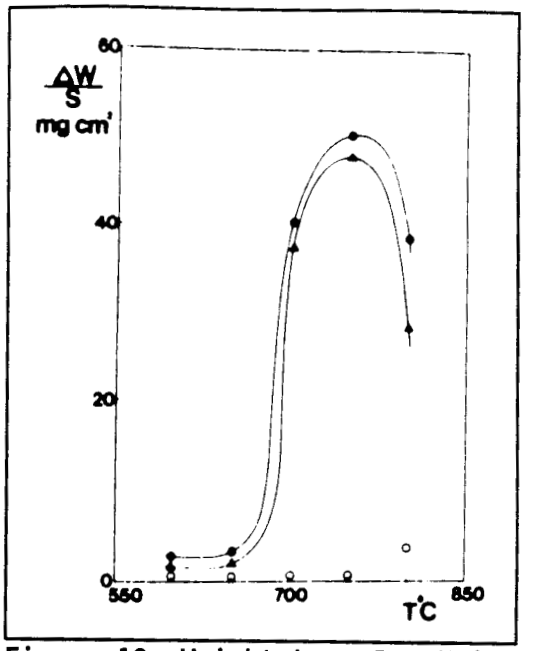

Figure 18 Weight Loss Per Unit Area vs. Temperature (HT-91)

Legend:

▲ 50 h (with salt); • 100 h (with salt); ○ 100 h (without salt)

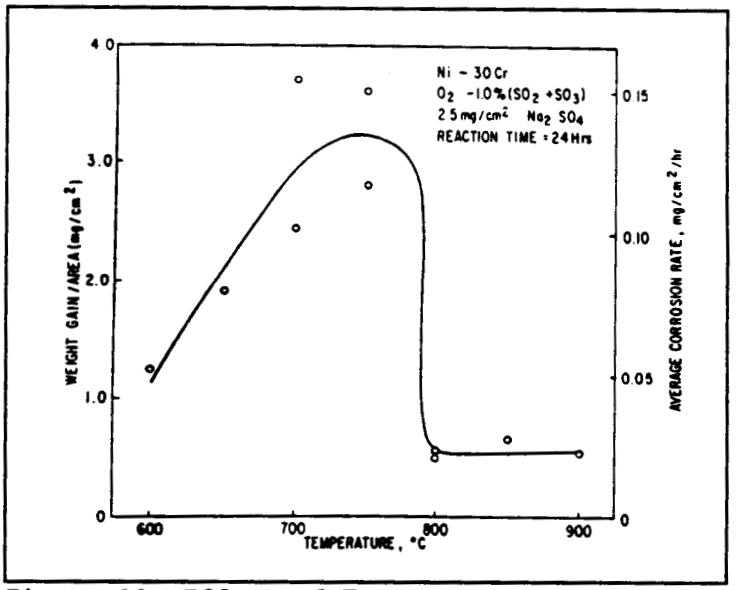

Figure 19 Effect of Temperature on the Corrosion Rate of Ni-30Cr, Coated With 2.5 mg/cm² of Na_2SO_4, in O_2-1% (SO_2 + SO_3)

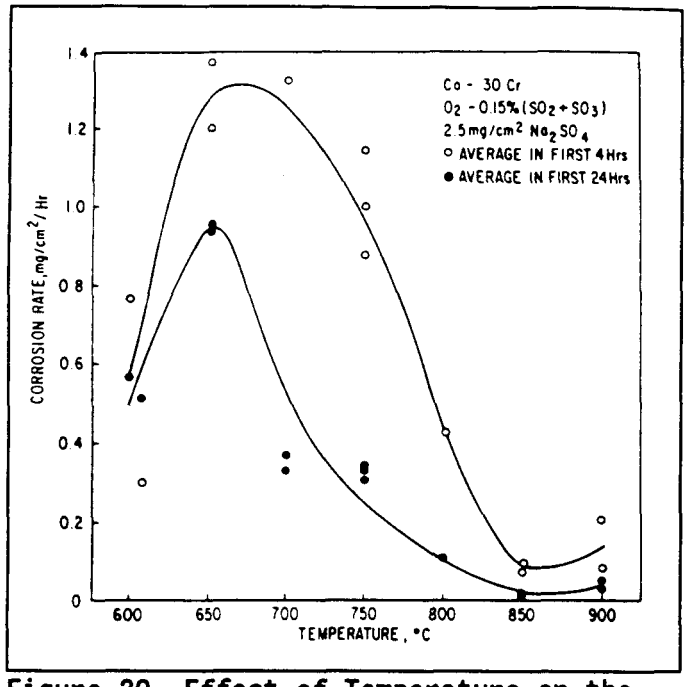

Figure 20 Effect of Temperature on the Corrosion Rate of Co-30Cr, Coated With 2.5 mg/cm² of Na_2SO_4, in O_2-0.15% (SO_2 + SO_3)

W. Wolowodiuk, S. Kihara, and K. Nakagawa [15] conducted a fireside corrosion testing program to extend the work of Rehn [14]. The range of materials examined included tubing alloys, cladding alloys, weld alloys, chromized metals, and a magnesium zirconate plasma coating. The complete test matrix used in this study comprised over 2100 different tests. Tests were conducted for 100 hours at 1112, 1200, 1292, and 1382°F (600, 650, 700, and 750°C). Synthetic coal ash and flue gas were used in the tests. To determine the effect of environmental variables on the corrosion behavior of different alloys, the levels of SO_2 and O_2 in the flue gas and the level of alkali sulfates in the synthetic coal ash were modified in various experiments. The SO_2 level in the flue gas was varied between 0.05 and 1.0 vol%; two levels of O_2 were also used--2 and 4 vol%. The balance of the flue gas was 10 vol% H_2O, 15 vol% CO_2, and N_2. Alkali sulfates consisted of K_2SO_4 and Na_2SO_4 in a 1:1 ratio, with the alkali level adjusted to 2.5, 5.0, or 10.0 wt%. The balance of the ash was Fe_2O_3, Al_2O_3, and SiO_2 in a 1:1:1 ratio. Tables 12, 13, and 14 list the alloys used in this project.

Table 12 Chemical Composition of Tube Alloys

Alloy \ Element	C	Si	Mn	P	S	Cu	Ni	Cr	Mo	Ti	Al	Nb	Co	V	B	N	Fe
347H	0.08	0.49	1.48	0.025	0.006	-	12.6	18.4	-	-	-	0.78	-	-	-	-	Bal
17-14CuMo	0.11	0.45	0.75	0.025	0.004	2.97	14.0	15.5	2.41	0.21	-	0.41	-	-	-	-	Bal
Esshete 1250	0.11	0.41	6.00	0.021	0.005	-	12.2	16.1	1.19	-	-	0.87	-	0.22	-	-	Bal
Alloy 800H	0.08	0.55	1.17	0.019	0.001	-	32.7	21.1	-	0.50	0.52	-	-	-	-	-	Bal
Alloy 800H(Nb mod.)	0.06	0.52	1.20	0.004	0.001	-	35.7	22.8	1.22	-	-	0.49	-	-	0.001	-	Bal
Inconel 617	0.06	0.41	0.37	0.006	0.002	-	Bal	22.0	8.53	0.38	1.15	-	12.5	-	-	-	-
Tempaloy A-1	0.09	0.49	1.58	0.020	0.004	-	10.8	18.0	-	0.07	-	0.15	-	-	-	-	Bal
12R72	0.10	0.49	1.82	0.008	0.011	-	14.9	14.8	1.19	0.47	-	-	-	-	0.007	-	Bal
Tempaloy CR30A	0.06	0.27	0.20	-	-	-	51.0	30.5	2.11	0.18	0.14	-	-	-	-	-	Bal
HR3C	0.06	0.39	1.26	0.012	0.001	-	20.1	24.6	-	-	-	0.47	-	-	-	0.245	Bal
T91	0.01	0.39	0.40	0.012	0.004	-	0.1	8.4	0.95	-	-	0.079	-	0.21	-	0.039	Bal

Table 13 Chemical Composition of Cladding Alloys

Alloy \ Element	C	Si	Mn	P	S	Cu	Ni	Cr	Mo	Ti	Al	Nb	Co	V	B	N	Fe
310	0.07	0.63	1.67	0.008	0.002	-	21.2	24.7	-	0.01	-	-	-	-	-	-	Bal
310Nb	0.01	0.23	0.70	0.015	0.001	-	20.3	25.4	-	-	-	0.25	-	-	-	-	Bal
35Cr-45Ni	0.07	0.03	0.01	0.002	0.003	-	45.3	35.5	-	-	0.11	0.59	-	-	-	-	Bal
314	0.08	1.90	1.28	0.023	0.001	-	20.0	24.9	-	-	-	-	-	-	-	-	Bal
Alloy 4C	0.05	2.6	4.9	0.005	0.010	0.03	20.0	19.5	-	-	1.4	-	-	-	-	-	Bal
253MA	0.09	1.73	0.32	0.014	0.001	-	11.0	21.0	-	-	-	-	-	-	-	0.18	Bal
Inconel 671	0.05	-	-	-	-	-	Bal	48.0	-	-	-	-	-	-	-	-	-

Table 14 Chemical Composition of Welding Alloys

Alloy \ Element	C	Si	Mn	P	S	Cu	Ni	Cr	Mo	Ti	Al	Nb	Co	V	B	N	Fe
347H	0.05	0.42	2.08	0.026	0.005	-	9.7	19.5	-	-	-	0.83	-	-	-	-	Bal
17-14CuMo	0.13	0.13	1.72	0.005	0.001	3.24	14.3	15.9	2.51	0.026	-	0.53	-	-	-	-	Bal
310	0.05	0.38	1.82	0.021	0.004	-	20.9	26.2	-	-	-	-	-	-	-	-	Bal
253MA	0.06	1.67	0.52	0.012	0.005	0.04	10.2	20.8	0.03	-	-	-	-	-	-	0.15	Bal
INCO 82	0.01	0.18	2.84	0.003	0.001	0.02	Bal	18.9	-	0.41	-	2.50	-	-	-	-	-
Inconel 617	0.07	0.21	0.14	-	0.001	0.15	Bal	22.1	9.0	0.30	1.06	-	12.1	-	-	-	2.54
Kobe 8126	0.07	0.25	0.57	0.002	0.003	-	Bal	40.5	-	-	-	-	-	-	-	-	5.22

General corrosion occurred on all of the alloys. No pitting was observed on any of the alloy specimens, either visually or microscopically. Weight-loss measurements were used to gauge the amount of wastage occurring on the specimens.

Figures 21 through 25 display an average weight loss calculated for all test conditions plotted against the test temperature. Figures 21, 22, and 23 illustrate the corrosion behavior of alloys with little, medium, and high corrosion resistance respectively. Each group of alloys produced a bell-shaped curve. All low-resistance alloys (Figure 21) contained molybdenum, and all suffered the highest corrosion rate at the same temperature [1292°F (700°C)]. All alloys with a medium corrosion resistance (Figure 22) contained about 18 percent chromium. The corrosion rate of the medium-resistance alloys peaked between 1200 and 1292°F (650°C and 700°C)--a lower temperature than that of the low resistance alloys. Alloys highly resistant to coal-ash corrosion (Figure 23) contained over 20 percent chromium. These alloys showed a sharp peak in their corrosion rate at 650°C.

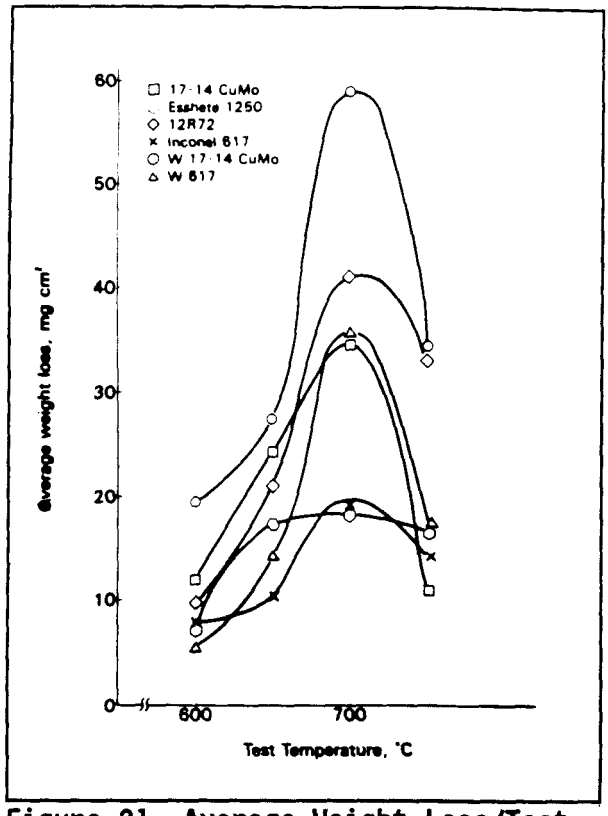

Figure 21 Average Weight Loss/Test Temperature Curves (Type 1)

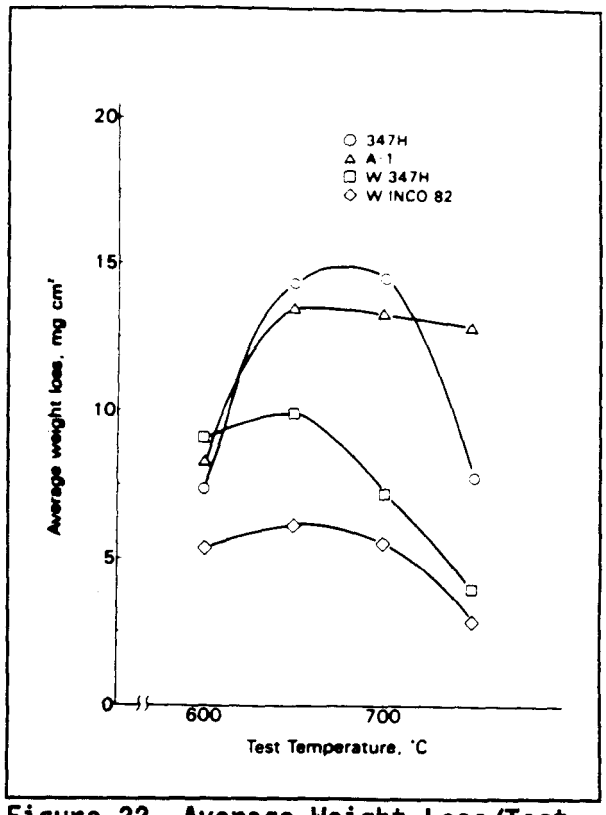

Figure 22 Average Weight Loss/Test Temperature Curves (Type 2)

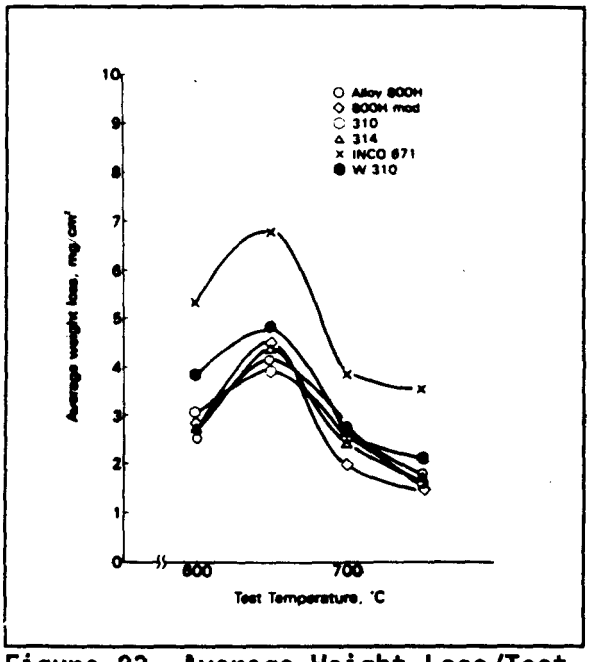

Figure 23 Average Weight Loss/Test Temperature Curves (Type 3)

Figures 24 and 25 display weight loss data against temperature for highly resistant alloys. In comparison with Figure 23, these alloys do not show a bell-shaped dependence of corrosion rate with temperature at the temperatures evaluated. The alloys illustrated in Figure 24 suffered less weight loss as the temperature rose. The alloys illustrated in Figure 25 showed no trend whatsoever. The behavior of either group of alloys cannot be explained by any known theory of molten alkali-iron trisulfate attack; however, both sets of alloys had the following in common:

- Almost no molten salts were formed on the metal surface.
- Heavy corrosion did occur at some test conditions.

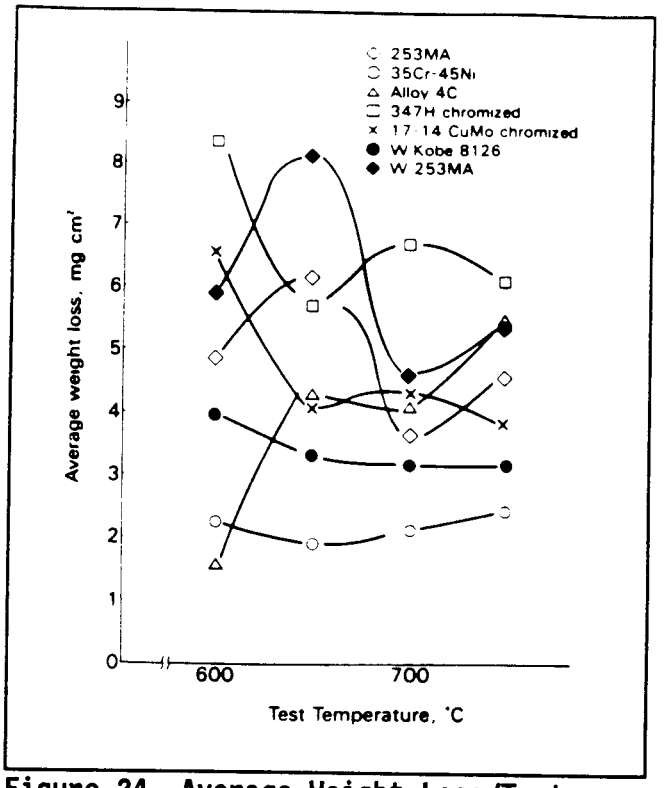

Figure 24 Average Weight Loss/Test Temperature Curves (Type 4)

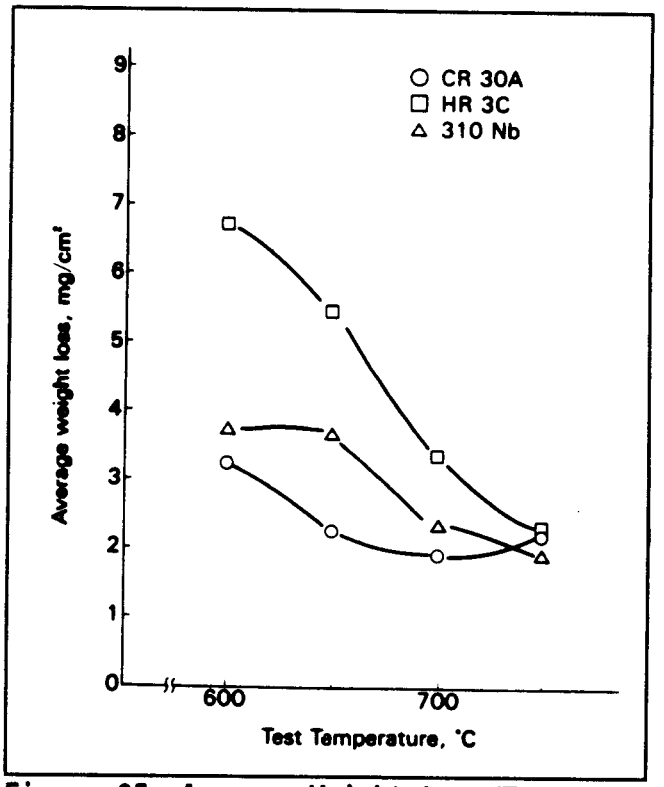

Figure 25 Average Weight Loss/Test Temperature Curves (Type 5)

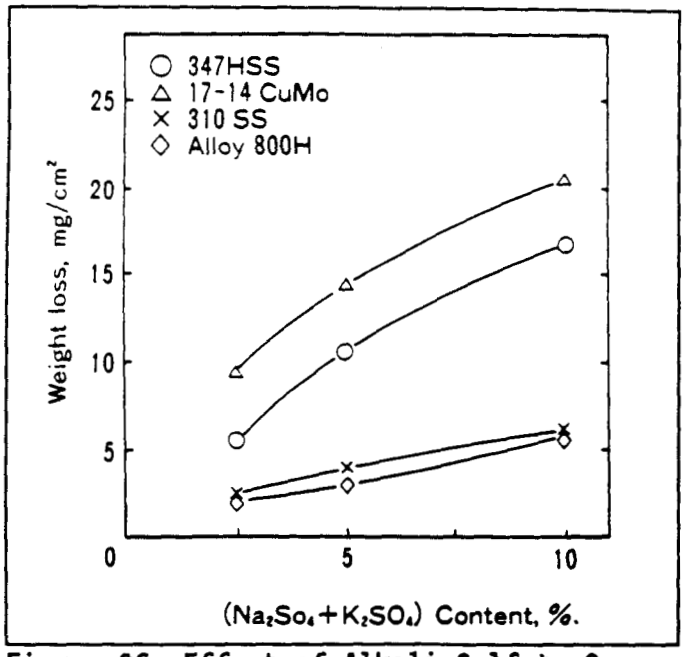

Figure 26 Effect of Alkali Sulfate Content on Corrosion Loss in 0.25 vol% SO_2 and 4 vol% O_2 Gas at 1202°F (650°C) for Type 347H, 17-14 CuMo, Type 310SS, and Alloy 800H

Changes in environmental variables changed the wastage of the alloys tested. An increase in the percentage of alkali sulfates in the synthetic coal ash increased the weight loss in an almost linear fashion (Figure 26). Additions of CaO to the synthetic ash tended to inhibit the formation of alkali-iron trisulfates by formation of $(Na,K)_2Ca_2(SO_4)$. These additions controlled weight losses of the low-resistance alloys, but they had little effect on the highly resistant alloys. An increase in the percentage of SO_2 in the gas stream likewise increased the alloy weight loss, but to a lesser extent than the alkali-sulfate dependence (Figure 27). Less-resistant alloys had a greater sensitivity to the percentage of SO_2 than the highly resistant alloys. The percentage of O_2 in the gas stream did not exert much influence over the corrosion rates.

Chromized alloys and metals coated with plasma-sprayed $MgZrO_2$ could not be evaluated strictly by weight loss; metallographic examination of the coatings was also conducted to determine the type and extent of coating deterioration. Chromized alloys showed pitting in several instances (chromized 17-14 CuMo and chromized T-91). Losses on all chromized alloys were significantly lower than on their untouched counterparts; however, how long the chromized layer will last is not clear. Plasma-sprayed $MgZrO_2$ coatings were permeable to molten sulfates. Examination of $MgZrO_2$-coated specimens after exposure showed a layer of corrosion products between the coating and the base metal. The thickness of the corrosion product layer was dependent upon the aggressiveness of the environment.

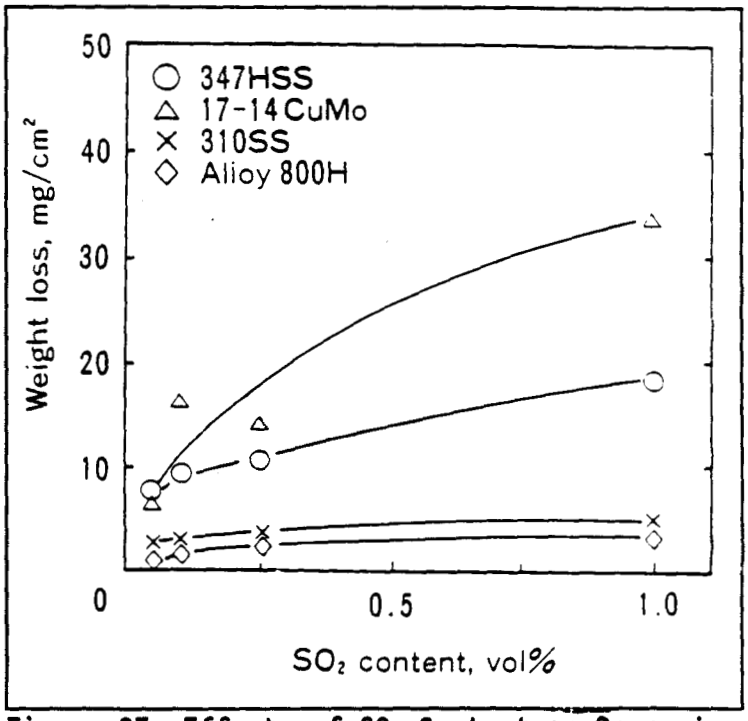

Figure 27 Effects of SO_2 Content on Corrosion Loss in 5 wt% Alkali Sulfates Ash at 1202°F (650°C) for Type 347H, Type 310SS, 17-14 CuMo, and Alloy 800H

Figure 28 compares chromium content in an alloy with the amount of wastage the alloy suffers. Alloys with at least 20 percent chromium show much greater resistance to alkali-iron trisulfate attack than alloys with a lower chromium content. An exception to the trend of increasing corrosion resistance with chromium content is Inconel 617. The high wastage of Inconel 617 may be due to its high molybdenum content. The high corrosion resistance of Esshete 1250 for its low chromium content may be due to its high manganese content (6 percent). Manganese is known to increase the adherence of the scale. No beneficial effects were found for additions of aluminum or silicon. Alloy 4C, which proved to be highly resistant for its chromium level in Rehn's study [14] performed no better than INCO 82, which has the same chromium content, but not the high level of aluminum or silicon.

A goal of laboratory testing is to develop a data base and a model to explain and predict coal-ash corrosion. Isocorrosion curves plot corrosion rates as a function of alkali sulfate and SO_2 concentration for a given alloy at a given temperature. They can be a powerful tool to validate the experiments using synthetic ash and flue gas against corrosion rates measured in operating boilers and to predict corrosion rates in New or existing boilers when the coal is operating conditions are changed.

Figure 29 is a representative isocorrosion diagram. The wastage rates were calculated by extrapolation from 100-hour test data and interpolation between points. The ranges of sulfur and alkalis for typical coals are superimposed on the isocorrosion diagram. Two levels of alkali content are plotted--the total alkali content of the coal and the acid-soluble alkali content of the coal. Shigeta, et al. demonstrated that only acid-soluble alkalies are responsible for the alkali-trisulfate attack [15]. One point from an in-plant test is plotted; the observed corrosion rate closely matches the rate predicted for the sulfur and acid-soluble alkali levels of the coal being burned.

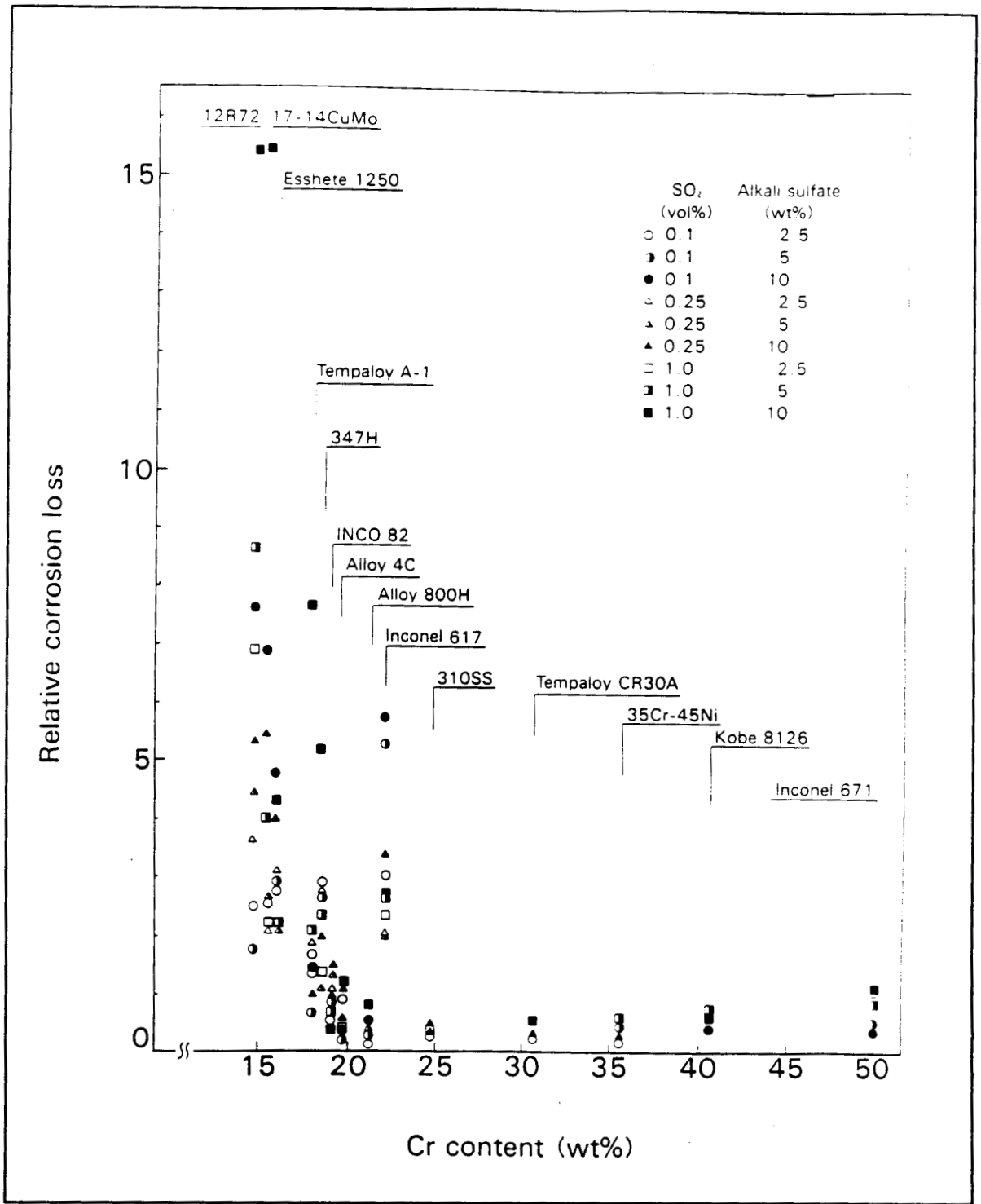

Figure 28 Relationship Between Chromium Content of Alloys and Relative Corrosion Loss in 4 vol% O_2 at 1292°F (700°C)

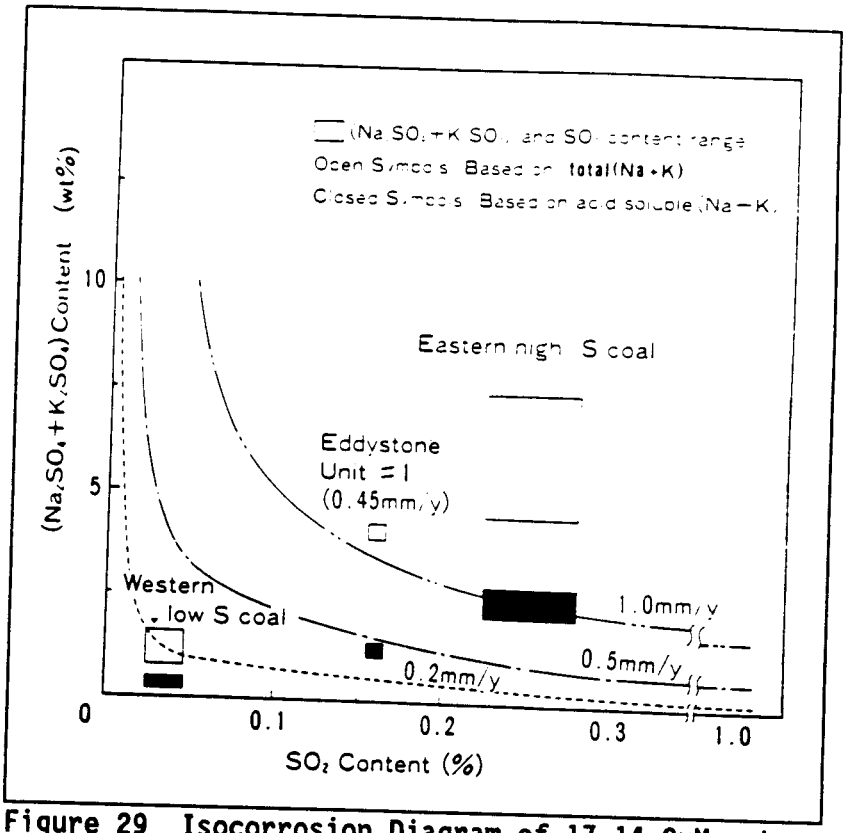

Figure 29 Isocorrosion Diagram of 17-14 CuMo at 1112°F (600°C)

Section 5

CONCLUSIONS AND STATE OF THE ART

After 40 years of development aimed at handling the problem of alkali-iron trisulfate attack, no easy solutions have been found. Supercritical units have required superheaters and reheaters constructed of expensive high-chromium/high-nickel alloys, and they have been limited to burning coals with low corrosivity. This form of corrosion will always be a concern for manufacturers and operators of pulverized-coal-fired boilers but corrosion research and alloy development has progressed to alleviate the catastrophic problem.

The basic mechanisms of alkali-iron-trisulfate attack in a coal combustion atmosphere were well-documented by researchers in the 1960s and 1970s, specifically the pioneering work by Nelson and Cain [17] and the studies conducted by Reid [18,19]. Definition of the species involved in the attack and transport through the liquid phase is being refined. Further research is needed to develop the predictive model for the sulfate systems involved in attack before any comprehensive quantitative theory can be developed.

With the exception of present work at ORNL, new alloy development has been largely through the efforts of several Japanese firms. Several high-chromium alloys, such as Type 310 and CR35A, hold promise as claddings for tubes in highly corrosive conditions. Modified lower-alloy steels--HR3C and CR30A, for example--with much greater corrosion resistance and creep-rupture strength are being developed. Rehn developed a modification of Type 347 stainless steel and several modifications of Alloy 4, (Al, Mn, Si) which exhibited better corrosion resistance than the parent alloy in laboratory tests with very aggressive alkali sulfates [14]. Subsequent testing by Wolowodiuk, Kihara, and Nakagawa, using an ash with a lower alkali content, did not substantiate Rehn's findings, however [15].

The beneficial effects of chromium have been demonstrated during laboratory experiments and in-situ probe trials. Corrosion resistance of various alloys subjected to coal ash with a wide range of sulfur and alkali levels correlates well with chromium content. Several studies indicate that little further corrosion resistance is furnished above a certain chromium content. However, the plateau for the benefit is still not clear. Molybdenum has been found detrimental in several studies. Large additions of molybdenum to either the alloy or the ash markedly decrease the corrosion resistance of the alloy; however, small additions of molybdenum do not seem to have much effect. The effects of various minor alloying elements is still being debated. Both beneficial and deleterious effects have been reported for aluminum, silicon, manganese, and various rare earths.

Corrosion-resistant coatings have shown promise in both laboratory corrosion studies and in-situ tests. Plasma-sprayed coatings of magnesium zirconate are almost impervious to corrosive attack from the higher melting compound that solidifies in the pores of the coating. However, these coatings spall and delaminate from the base metal. Diffusion coatings, such as chromizing and aluminizing, are resistant to spalling and have performed well in some circumstances. The performance of both sprayed and diffusion coatings is highly dependent upon the method of application, the length of the test, and the aggressiveness of the alkali sulfate. Short laboratory experiments may overstate the

abilities of coatings. A large data base of corrosion information has been assembled into isocorrosion diagrams that provide an isocorrosion line as a function of SO_2 and alkali sulfate level. The curves are drawn for a specific alloy at a specific temperature. The laboratory- derived curves were compared with field-measured corrosion rates, and the correlation appears promising. The validity of the curve should be further evaluated because the isocorrosion diagram is potentially a good quantitative engineering tool for predicting coal-ash corrosion on the basis of coal quality.

The laboratory coal-ash corrosion retort/field corrosion probe combination has proved valuable for coal-ash corrosion research. The laboratory test provides the accelerated screening device for alloy, temperature, and ash/gas constituent evaluation. The coal-ash corrosion probes exposed in operating utility boilers provide combined variables, complex gas/solids, heat-transfer conditions, etc., which are very difficult--if not impossible--to totally simulate in the laboratory. The combined coal analysis and metals exposure in laboratory and field advances the mechanist models for coal-ash corrosion; it also keeps research current as it relates to the realistic fuel variations that are a part of our changing technology and economic environment.

Section 6

REFERENCES

1. I. M. Rehn, "Improved Materials for Coal-Fired Boiler Superheater and Reheater Tubes Subjected to Fireside Corrosion," High Temperature Corrosion in Energy Systems (M. F. Rothman, ed.) The Metallurgical Society of AIME, Warrendale, Pennsylvania, 1985, pp. 377-388.

2. P. L. Rittenhouse, et al., "Assessment of Materials Needs for Advanced Steam Cycle Coal-Fired Plants" prepared by ORNL for the U.S. DOE under Contract No. DE-AC05-840R21400, August 1985.

3. I. M. Rehn, "Corrosion Problems in Coal Fired Boiler Superheater and Reheater Tubes," Foster Wheeler Development Corporation, Livingston, New Jersey, EPRI CS-1653, 1980.

4. I. M. Rehn, "Fireside Corrosion of Superheater Alloys for Advanced Cycle Steam Plants," Foster Wheeler Development Corporation, Livingston, New Jersey, EPRI 5195, 1987.

5. Foster Wheeler Energy Corporation, "Design of Improved Materials Systems for Coal-Fired Boiler Superheater and Reheater Tubes," FWEC 0-59-8008, response to Electric Power Research Institute's RFQ 1300, September 1975.

6. D. B. Meadowcroft "An Introduction to Fireside Corrosion Experience in the Central Electricity Generating Board" Werkstoffe und Korrosion, No. 39, 1988, pp. 45-48.

7. T. Flatley and C. W. Morris, "UK Corrosion '83," Proceedings of the Corrosion Conference, November 1982.

8. E. P. Latham, T. Flatley, and C. W. Morris, "Comparative Performance of Superheated Steam Tube Materials in Pulverized Fuel Fired Plant Environments" in Corrosion Resistant Materials for Coal Conversion Systems, D. B. Meadowcroft and M. I. Manning, eds., Applied Science Publishers, New York, 1983.

9. U. Balting, et al., "Fireside Corrosion and Ferritic/Austenitic Steels and High-Alloy Materials for Superheaters, Especially Reheaters of Coal-Fired Steam Generators," Werkstoffe und Korrosion, No. 39, 1988, pp. 90-97.

10. D. B. Meadowcroft, "High Temperature Corrosion of Alloys and Coatings in Oil- and Coal-Fired Boilers," Materials Science and Engineering, No. 88, 1987, pp. 313-320.

11. P. E. Chandler and M. B. C. Quigley, "The Application of Plasma Sprayed Coatings for the Protection of Boiler Tubing," Advances in Thermal Spraying: Proceedings of the 11th International Conference, Montreal, September 1986.

12. D. W. Locklin, et al., "Electric Utility Use of Fireside Additives," Battelle Columbus Laboratories, EPRI CS-1318, January 1980.

13. J. F. DeLong, et al., "Metallurgical Examination After One Year of Service of Experimental 17-14 CuMo I.D./O.D. Chromized and TP310 Clad Tubing Installed in Eddystone Unit No. 1," ASME Conference on Coatings and Bimetallics for Energy Systems and Chemical Process Environments, South Carolina, November 1984.

14. I. M. Rehn, Laboratory Fire-Side Corrosion Evaluation of Improved Superheater Tube Alloys and Coatings, EPRI CS-3134, June 1983.

15. W. Wolowodiuk, S. Kihara, and K. Nakagawa, "Laboratory Coal Ash Corrosion Tests," EPRI GS-6449, July 1989.

16. Foster Wheeler Development Corportation, "TVA Gallatin Unit 2: Coal-Ash Corrosion Probes (4000-Hour Test Results), "prepared for the Electric Power Research Institute under EPRI Contrat RP1403-19, Boiler R&D for Improved Coal-Fired Power Plants, October 1989.

17. Foster Wheeler Development Corportation, "TVA Crist Unit 2: Coal-Ash Corrosion Probes (4000-Hour Test Results), "prepared for the Electric Power Research Institute under EPRI Contrat RP1403-19, Boiler R&D for Improved Coal-Fired Power Plants, October 1989.

18. W. Nelson and C. Cain, Jr., "Corrosion of Superheaters and Reheaters of Pulverized-Coal-Fired Boilers," Transactions of the ASME, Journal of Engineering for Power, July 1960, pp. 194-204.

19. W. T. Reid, "Formation of Alkali Iron Trisulphates and Other Compounds Causing Corrosion in Boilers and Gas Turbines," Project Review July 1, 1966 - June 30, 1968, prepared by Battelle Memorial Institute, Columbus, Ohio, June 1968.

20. W. T. Reid, External Corrosion and Deposits: Boilers and Gas Turbines, American Elsevier Publishing Company, New York, 1974.

21. G. J. Hills, "Corrosion of Metals by Molten Salts," Proceedings of the Marchwood Conference: Mechanism of Corrosion by Fuel Impurities, Johnson and Littler (eds.), Butterworths, London, 1963.

22. A. Hendry and D. J. Lees, "Corrosion of Austenitic Steels in Molten Sulphate Deposits," Corrosion Science, Vol. 20, 1980, pp. 383-404.

23. P. Nanni, et al., "Sodium Sulphate Induced Hot Corrosion of Pure Fe, Mn, and Cr in Combustion Gas," Key Engineering Material, Vol. 20-29, No. 4, 1988, pp. 3413-3422.

24. F. Gesmundo and F. Viani, "The Mechanism of the Low-Temperature Hot Corrosion of Pure Iron and Manganese at 600-800°C," Materials Chemistry and Physics, Vol. 20, 1988, pp. 513-528.

25. K. Lillerud and P. Kofstad, "Sulphate Induced Hot Corrosion of Nickel," Oxidation of Metals, 1984, pp. 233-270.

26. S. Kihara, et al., "Simulating Test Results for Fireside Corrosion of Superheater and Reheater Tubes Operated at Advanced Steam Condition in Coal Fired Boilers" in High Temperature Corrosion in Energy Systems, (M. F. Rothman, ed.), Metallurgical Society of the AIME, Warrendale, Pennsylvania, 1985, pp. 361-376.

27. M. Tamura, et al., "High Temperature Performance of 35Cr-45Ni-Fe Alloy," High Temperature Corrosion in Energy Systems, M. F. Rothman (ed.), Metallurgical Society of the AIME, Warrendale, Pennsylvania, 1985, pp. 389-403.

28. M. Tamura, et al., "Promising Alloys for the Heat Exchangers of Advanced Coal Fired Boilers," Industrial Heat Exchangers Conference, Pittsburgh, November 1985.

29. K. Nakagawa, et al., "Electrochemical Evaluation of Chromized Type 347H and Chromized 17-14 CuMo Steel in Coal Ash Corrosion Atmosphere," Conference Proceedings of the ASM, R. D. Sisson (ed.), 1984, pp. 77-87.

30. K. Nakagawa, et al., "Electrochemical Evaluation of Superheater Materials in Coal Ash Corrosion Atmospheres," ASME Paper 83-JPGC-Pwr-83, Joint Power Generation Conference, 1983.

31. F. Gesmundo and P. Nanni, "Low Temperature Hot Corrosion of Two Low Chrominum Commercial Steels," 8th European Congress on Corrosion, Paris, November 1985.

32. K. L. Luthra and D. A. Shores, "Mechanism of Na_2SO_4 Induced Corrosion at 600 - 900°C", Journal of the Electrochemical Society: Solid State Science and Technology, October 1980, pp. 2202-2210.

Appendix A

DISTRIBUTION

AIR PRODUCTS AND CHEMICALS
P. O. Box 538
Allentown, PA 18105
S. W. Dean
S. C. Weiner

ALBERTA RESEARCH COUNCIL
Oil Sands Research Department
P.O. Box 8330, Postal Station F
Edmonton, Alberta
Canada T6H5X2
L. G. S. Gray

ALLISON GAS TURBINE DIVISION
P. O. Box 420
Indianapolis, IN 46206-0420
P. Khandelwal (Speed Code W-5)
R. A. Wenglarz (Speed Code W-16)

AMAX R&D CENTER
5950 McIntyre Street
Golden, CO 80403
T. B. Cox

ARGONNE NATIONAL LABORATORY
9700 S. Cass Avenue
Argonne, IL 60439
W. A. Ellingson
K. Natesan

ARGONNE NATIONAL LABORATORY-WEST
P. O. Box 2528
Idaho Falls, ID 83403-2528
S. P. Henslee

AVCO RESEARCH LABORATORY
2385 Revere Beach Parkway
Everett, MA 02149
R. J. Pollina

BABCOCK & WILCOX
1562 Beeson St.
Alliance, OH 44601
T. I. Johnson

BABCOCK & WILCOX
Domestic Fossil Operations
20 South Van Buren Ave.
Barberton, OH 44023
M. Gold

BATTELLE-COLUMBUS LABORATORIES
505 King Avenue
Columbus, OH 43201
V. K. Sethi

BETHLEHEM STEEL CORPORATION
Homer Research Laboratory
Bethlehem, PA 18016
B. L. Bramfitt
J. M. Chilton

BRITISH COAL CORPORATION
Coal Research Establishment
Stoke Orchard, Cheltenham
Glouchester, England GL52 4RZ
M. Arnold
C. Bower
A. Twigg

BRITISH GAS CORPORATION
Westfield Development Centre
Cardenden, Fife
Scotland KY50HP
J. E. Scott

BROOKHAVEN NATIONAL LABORATORY
Department of Applied Science
Upton, Long Island, NY 11973
T. E. O'Hare

CANADA CENTER FOR MINERAL & ENERGY TECHNOLOGY
568 Booth Street
Ottawa, Ontario
Canada K1A OG1
R. Winston Revie
Mahi Sahoo

CASE WESTERN RESERVE UNIVERSITY
Department of Metallurgy & Materials Science
516 White Building
10900 Euclid Avenue
Cleveland, OH 44106
K. M. Vedula

COLORADO SCHOOL OF MINES
Department of Metallurgical Engineering
Golden, CO 80401
G. R. Edwards

COMBUSTION ENGINEERING
911 W. Main Street
Chattanooga, TN 37402
D. A. Canonico

EC TECHNOLOGIES INC.
3614 Highpoint Drive
San Antonio, TX 78217
D. J. Kenton

ELECTRIC POWER RESEARCH INSTITUTE
P.O. Box 10412
3412 Hillview Avenue
Palo Alto, CA 94303
W. T. Bakker
J. T. Stringer
R. L. S. Chang
H. Wolk

EUROPEAN COMMUNITIES JOINT RESEARCH CENTRE
Petten Establishment
P. O. Box 2
1755 ZG Petten
The Netherlands
M. Van de Voorde

GENERAL ELECTRIC COMPANY
1 River Road
Bldg. 55, Room 115
Schenectady, NY 12345
R. W. Haskell

IDAHO NATIONAL ENGINEERING LABORATORY
P.O. Box 1625
Idaho Falls, ID 83415
R. N. Wright

LAWRENCE LIVERMORE LABORATORY
P.O. Box 808, L-325
Livermore, CA 94550
W. A. Steele

LOS ALAMOS NATIONAL LABORATORY
P. O. Box 1663
Los Alamos, NM 87545
P. D. Shalek

NATIONAL INSTITUTE OF STANDARDS AND TECHNOLOGY
Materials Building
Gaithersburg, MD 20899
S. J. Dapkunas
L. K. Ives

NATIONAL MATERIALS ADVISORY BOARD
National Research Council
2101 Constitution Avenue
Washington, DC 20418
K. M. Zwilsky

NEW ENERGY DEVELOPMENT ORGANIZATION
Sunshine 60 Bldg.
P.O. Box 1151, 1-1
Higashi-Ikebukuro 3-chrome
Toshima-Ku, Tokyo, 170
Japan
S. Ueda

OAK RIDGE NATIONAL LABORATORY
P. O. Box 2008
Oak Ridge, TN 37831
D. N. Braski
P. T. Carlson
W. N. Drewery, Jr. (8 copies)
R. R. Judkins
R. W. Swindeman

RESEARCH TRIANGLE INSTITUTE
P. O. Box 12194
Research Triangle Park, NC 27709
T. W. Sigmon

SHELL DEVELOPMENT COMPANY
P. O. Box 1380
Houston, TX 77251-1380
L. W. R. Dicks

THE JOHNS HOPKINS UNIVERSITY
Materials Science & Engineering
Maryland Hall
Baltimore, MD 21218
R. E. Green, Jr.

THE MATERIALS PROPERTIES COUNCIL, INC.
United Engineering Center
345 E. Forty-Seventh Street
New York, NY 10017
M. Prager

THE TORRINGTON COMPANY
Advanced Technology Center
59 Field Street
Torrington, CT 06790
W. J. Chmura

UNION CARBIDE CORPORATION
Linde Division
P. O. Box 44
175 East Park Drive
Tonawanda, NY 14151-0044
Harry Cheung

UNITED ENGINEERS & CONSTRUCTORS
30 South 17th Street
P. O. Box 8223
Philadelphia, PA 19101
A. J. Karalis

UNIVERSAL ENERGY SYSTEMS, INC.
4401 Dayton-Zenia Road
Dayton, OH 45432
V. Srinivasan

UNIVERSITY OF CALIFORNIA AT BERKELEY
Department of Materials Science
and Mineral Engineering
Berkeley, CA 94720
R. O. Ritchie

UNIVERSITY OF NOTRE DAME
Department of Materials Science
and Engineering
P. O. Box E
Notre Dame, IN 46556
T. H. Kosel

UNIVERSITY OF TENNESSEE AT KNOXVILLE
Materials Science and Engineering Dept.
Knoxville, TN 37996
C. D. Lundin

UNIVERSITY OF TENNESSEE SPACE INSTITUTE
Tullahoma, TN 37388
J. W. Muehlhauser

UNIVERSITY OF WASHINGTON
Department of Materials Science
and Engineering
101 Wilson, FB-10
Seattle, WA 98195
T. G. Stoebe

WESTINGHOUSE ELECTRIC CORPORATION
Research and Development Center
1310 Beulah Road
Pittsburgh, PA 15235
S. C. Singhal

WESTINGHOUSE HANFORD COMPANY
P.O. Box 1970, W/A-65
Richland, WA 99352
R. N. Johnson

DOE
OAK RIDGE OPERATIONS OFFICE
P. O. Box 2001
Oak Ridge, TN 37831
Assistant Manager for Energy Research
and Development
E. E. Hoffman

DOE
OFFICE OF BASIC ENERGY SCIENCES
Materials Sciences Division
ER-131 GTN
Washington, DC 20545
J. B. Darby

DOE
OFFICE OF CONSERVATION AND RENEWABLE
ENERGY
Energy Conversion and Utilization Technologies
CE-12 Forrestal Building
Washington, DC 20545
J. J. Eberhardt

DOE
OFFICE OF FOSSIL ENERGY
Washington, DC 20545
D. J. Beecy (FE-14) GTN
J. P. Carr (FE-14) GTN
F. M. Glaser (FE-14) GTN
T. B. Simpson (FE-25) GTN

DOE
MORGANTOWN ENERGY TECHNOLOGY
CENTER
P. O. Box 880
Morgantown, WV 26505
R. A. Bajura
R. C. Bedick
F. W. Crouse, Jr.
N. T. Holcombe
W. J. Huber
M. J. Mayfield
J. E. Notestein
J. S. Wilson

DOE
PITTSBURGH ENERGY TECHNOLOGY CENTER
P. O. Box 10940
Pittsburgh, PA 15236
S. Akhtar
T. C. Rupel
R. Santore
T. M. Torkos